

DISS. ETH No. 14306

# Optical Probing of Single-Molecule Interactions

A dissertation submitted to the

SWISS FEDERAL INSTITUTE OF TECHNOLOGY ZÜRICH

For the degree of  
Doctor of Natural Sciences

presented by  
WERNER TRABESINGER  
Dipl. Ing. Techn. Phys., University of Linz

born October 3, 1973  
Klagenfurt, Austria

Accepted on the recommendation of:  
Prof. Dr. Urs P. Wild, Examiner  
Prof. Dr. Vahid Sandoghdar, Co-Examiner  
Dr. Bert Hecht, Co-Examiner

2002

*To my parents*

# Contents

Acknowledgements . . . . .	v
Abstract . . . . .	vii
Zusammenfassung . . . . .	ix
<b>1 Introduction</b>	<b>1</b>
<b>2 Fundamentals of Single-Molecule Spectroscopy</b>	<b>7</b>
2.1 Photophysics of a Single Molecule . . . . .	8
2.2 Selectively Addressing Single Molecules . . . . .	10
2.3 Signal-to-Noise Ratio Considerations . . . . .	11
2.4 Specific Advantages of Single-Molecule Observations . . . . .	13
<b>3 Techniques and Concepts</b>	<b>15</b>
3.1 Microscopy Techniques . . . . .	16
3.1.1 Wide-Field Microscopy . . . . .	16
3.1.2 Scanning Confocal Optical Microscopy (SCOM) . . . . .	17
3.1.3 Atomic Force Microscopy . . . . .	21
3.2 Data Analysis Techniques . . . . .	23
3.2.1 Stoichiometric Quantitation of Cluster Sizes . . . . .	23
3.2.2 Superresolution Position Determination . . . . .	25
3.2.3 Determination of Single-Exponential Decay Rates by Averaging	27
<b>4 Tracing the Formation of a Molecular Polymer Blend</b>	<b>31</b>

4.1	Introduction . . . . .	32
4.1.1	Evidences for a Molecular Dispersion from Ensemble Experiments . . . . .	32
4.2	Single-Molecule Studies . . . . .	33
4.3	Experimental . . . . .	34
4.4	Results and Discussion . . . . .	35
4.5	Quantitative Analysis . . . . .	38
4.6	Deformation-induced Orientation . . . . .	41
4.7	Conclusions . . . . .	42
<b>5</b>	<b>Statistical Analysis of Single-Molecule Colocalization Assays</b>	<b>43</b>
5.1	Introduction . . . . .	44
5.2	Experimental . . . . .	45
5.3	Microscopy . . . . .	45
5.4	Theory . . . . .	47
5.5	Results and Discussion . . . . .	49
5.6	Conclusions . . . . .	54
<b>6</b>	<b>Continuous Real-Time Measurement of Fluorescence Lifetimes</b>	<b>57</b>
6.1	Introduction . . . . .	58
6.2	Experimental . . . . .	59
6.3	Theory . . . . .	60
6.4	Results and Discussion . . . . .	62
6.5	Conclusions . . . . .	64
<b>7</b>	<b>Fluorescence Lifetime of Molecules in Complex Surroundings</b>	<b>67</b>
7.1	Introduction . . . . .	68
7.2	Theory . . . . .	69
7.3	Results and Discussion . . . . .	71

---

7.4	Experimental Relevance . . . . .	73
<b>8</b>	<b>Single-molecule near-field optical energy transfer microscopy</b>	<b>75</b>
8.1	Introduction . . . . .	76
8.2	Experimental . . . . .	76
8.3	Alignment Procedure . . . . .	78
8.4	Results and Discussion . . . . .	79
8.5	Experiments with uncoated $Si_3N_4$ tips . . . . .	82
8.6	Conclusion . . . . .	83
	<b>Bibliography</b>	<b>85</b>
	<b>Curriculum Vitae</b>	<b>93</b>



## Acknowledgements

First of all, I would like to thank Prof. U. P. Wild for giving me the opportunity to work in his group. His financial support and his continuous loyalty provided the basis for this thesis.

Prof. Vahid Sandoghdar is acknowledged for stimulating suggestions and for kindly taking the role of co-examiner.

I am further indebted to Dr. Bert Hecht, who supervised me throughout my PhD thesis. His inexhaustible patience both for experimental setups and myself proved crucial at many points of my thesis. Much of what I learned about scientific work, I owe to him.

I had the pleasure to work with Dr. Beate Sick during the beginning of my time in the group, when the only room-temperature single-molecule setup was in her lab. I will always remember the exciting times, when we observed the first molecules on her confocal setup.

Dr. Axel Kramer, was a valuable source of encouragement and criticism for my near-field project. Not only does he share my passion for lock-in amplifiers and the design of peculiar electronic circuits, but also an ironical view of life as a "lab-rat".

Dr. Christian Hübner helped me bring time resolution to the G3-lab. His assistance and the loan of TCSPC equipment, added time-resolution to the G3-lab. His patience in reanimating my computer many times, deserves special mention. He and Axel turned out to be great friends and members of the G14-gang.

Dr. Max Kreiter, who joined the group only about a year ago, contributed greatly to my near-field work. His profound understanding of electrodynamics and the behaviour of molecules at interfaces helped me understand better my experimental work.

Dr. Gerhard Schütz was my lab-mate during the time in Linz. His excellent knowledge on statistics contributed greatly to the part of my work outlined in chapter 5. His and Prof. Thomas Schmidt's guidance during my diploma have initiated my passion for single molecules. I will always remember the time spent in Linz.

Dr. Andrea Montali and Prof. Christoph Weder were my coworkers in the polymer project. Their enthusiasm for single-molecule microscopy and their relentless efforts

in checking and rechecking sample preparation procedures were vital for what finally turned out to be a nice piece of work.

Special thanks goes to Herr Boss from the electronic workshop for repairing my NIM-modules countless times. His patience in explaining electronic circuits and the time spent together selecting amplifiers and many other compounds helped me a lot.

It goes without saying that the Wild-group with all of its former and current members was an excellent environment for my whole time in Zurich. The good atmosphere also extended beyond the workplace. As a result, we spent many nice BBQs and pub-evenings.

Last not least, I thank my parents for their continuous support not only during this thesis, but for the last 28 years.



# Abstract

The present thesis is concerned with the optical probing of interactions of individual molecules in complex surroundings. Examples for molecular interactions from three different fields of application are investigated: Materials sciences, receptor-ligand interactions in biological systems and near-field interactions of single molecules with metallic structures.

In chapter 2, requirements on the photophysical parameters of dye molecules and the experimental apparatus for single-molecule microscopy are derived from a photophysical rate-equation model. Chapter 3 introduces the three microscopy techniques used in the thesis, scanning confocal optical microscopy (SCOM), wide-field microscopy, and atomic force microscopy (AFM), as well as mathematical approaches used for data evaluation.

In chapter 4, a deformation-induced transition of a polymer blend system from a phase-separated state to a molecular dispersion is traced by means of SCOM. Stoichiometric analysis of cluster size distributions reveals that with increasing degree of tensile deformation, breaking up of molecular aggregates occurs. Concomitantly, the degree of orientation of the molecules increases as a result of strong interaction between isolated molecules and their surroundings.

Chapter 5 deals with the direct measurement of binding events at the level of individual ligands and receptors. Independent localization of both ligands *and* receptors with subdiffraction-limited accuracy yields intermolecular distance measurements with nm-accuracy. From first principles, a function is derived, which translates distances into probabilities for binding. Decision-making criteria, for obtaining

judgments on the basis of sets of observations and objective comparison between experiments are introduced.

A single-molecular interaction of particular interest with regard to near-field optics is the case of molecules in close proximity to metallic surfaces. The altered boundary conditions for the emitting molecular dipole lead to distinct variations of the fluorescence intensity and lifetime. In chapter 8, the implementation of an experiment is described, in which a metallized scanning probe tip is controllably approached to a fluorescence molecule, while intensity and lifetime are monitored continuously. Both parameters reveal that strong nonradiative transfer of the molecule to the metallic tip sets in at small distances, shortening the excited state lifetime.

# Zusammenfassung

Die vorliegende Arbeit beschäftigt sich mit der optischen Messung von Wechselwirkungen einzelner Moleküle in komplexen Umgebungen. Beispiele für molekulare Wechselwirkungen aus drei verschiedenen Gebieten werden behandelt: Materialwissenschaften, Rezeptor-Liganden Wechselwirkungen am Beispiel biologischer Systeme und Nahfeldwechselwirkungen einzelner Moleküle mit metallischen Strukturen.

Anforderungen an die photophysikalischen Parameter von Fluoreszenzmolekülen und den experimentellen Aufbau werden in Kapitel 2 aus einem Ratenmodell hergeleitet. Kapitel 3 gibt einen Überblick über die in dieser Arbeit verwendeten Techniken der Rasterkonfokalmikroskopie, der Weitfeldmikroskopie und der Atomkraftmikroskopie, sowie über Formalismen zur Auswertung der experimentellen Daten.

Kapitel 4 zeigt mittels Konfokalmikroskopie den deformationsinduzierten Übergang einer phasenseparierten Polymermischung zu einer molekularen Dispersion auf. Die stöchiometrische Analyse der Grösse der phasenseparierten Domänen zeigt auf, daß mit zunehmender Verstreckung ein Aufbrechen der molekularen Aggregate stattfindet. Gleichzeitig führt die zunehmende Wechselwirkung zwischen den isolierten Molekülen und Ihrer Umgebung zu einer uniaxialen Ausrichtung.

In Kapitel 5 wird die Beobachtung einzelner Bindungsereignisse zwischen Rezeptor- und Ligandenmolekülen behandelt. Die unabhängige Messung der Positionen von Rezeptor *und* Ligandenmolekülen mit nicht beugungsbegrenzter Genauigkeit ermöglicht es, intermolekulare Abstände auf einer nm-Skala zu bestimmen. Aus statistischen Überlegungen wird eine Funktion hergeleitet, die eine Zuordnung zwischen gemessenen Abständen und Bindungswahrscheinlichkeiten ermöglicht. Des weiteren

werden Kriterien zur Entscheidungsfindung auf der Basis weniger Beobachtungen und zum objektiven Vergleich zwischen Experimenten gegeben.

Im Hinblick auf die Nahfeldoptik ist die Wechselwirkung einzelner Moleküle in unmittelbarer Nähe zu metallischen Oberflächen von besonderem Interesse. Die geänderten Randbedingungen für den emittierenden Dipol führen zu Änderungen der Fluoreszenzintensität und Fluoreszenzlebensdauer. Kapitel 8 beschreibt ein Experiment, das die kontrollierte Annäherung einer metallbeschichteten Rastersonde an ein Fluoreszenzmolekül gestattet, während Fluoreszenzlebensdauer und -intensität ständig gemessen werden. Der Vergleich beider Parameter zeigt, daß bei kleinen Abständen zwischen Molekül und Metall effizienter strahlungsloser Energietransfer einsetzt, der zu einer Verkürzung der Lebensdauer des angeregten Zustands führt.

# 1. Introduction

Since the early days of modern science, it has been a dream to directly visualize the structure of matter at a microscopic scale [1]. The introduction of light microscopy by Zacharias Jansen (1595) permitted the examination of objects in the micron range, constituting an impressive breakthrough for the study of very small structures. For about three centuries, the technique remained essentially unchanged, until in the early 20<sup>th</sup> century, scientific interest was drawn to techniques of higher resolution, such as electron microscopy [2]. In the 1980s, the advent of scanning tunneling microscopy (STM) [3] and atomic force microscopy (AFM) [4] for the first time provided atomic-scale images of surfaces, generating intense excitement for the development of novel microscopies.

Only briefly after STM and AFM, single-molecule spectroscopy (SMS) [5] and scanning near-field optical microscopy (SNOM) [6] were introduced, demonstrating that subdiffraction-limited length scales and even single-molecular entities can be addressed optically. These new developments have initiated systematic studies of the behaviour of single fluorescence molecules in their nanoscale environment at cryogenic temperatures, revealing quantum phenomena, which are not observable for ensembles [7]. After the early years of SMS, where fundamental photophysical questions and solid state dynamics were at the center of interest, room-temperature single-molecule microscopy applications became increasingly popular [8].

In most room-temperature single-molecule microscopy applications, fluorescence molecules are used as labels. As individual molecular entities, they are influenced only by their immediate surroundings, in contrast to an ensemble of labels, which averages over the properties of a larger volume. Examination of the labels' molecular properties therefore can be used to probe single-molecular interactions in a nanoscopic environment. Monitoring of many molecular processes, as e.g. lateral and rotational diffusion [9, 10], or intramolecular conformational dynamics [11] is possible.

This thesis deals with the optical observation of single-molecular interactions in a complex environment. Single-molecule microscopy is applied for monitoring structural rearrangements in polymer-blend systems, individual biomolecular recognition events and near-field optical interactions of a single-molecule with a controllable

---

perturber. In all three topics treated within this thesis, the optical observation of fluorescence molecules provides information about locally occurring interaction processes on a nanometer scale.

The feasibility of single-molecule studies critically depends on the photophysical properties of the marker molecules. In chapter 2, the photophysics of single molecules at room temperature is discussed in terms of a rate-equation model. The results indicate the relevant molecular and experimental parameters for optimization of single-molecule experiments. The fundamental advantages of single-molecule studies over ensemble experiments are discussed.

Depending on the specific type of experiment, either the screening of many molecules in parallel, or the study of isolated molecules may be desired. For parallel screening of many molecules, standard wide-field microscopy is best suited. However, wide-field microscopy is limited to imaging thin samples, since it does not discriminate against light from out-of-focus regions. In cases, where such discrimination is required, scanning confocal optical microscopy (SCOM) is well suited and offers the additional capability of locally measuring fluorescence dynamics on a point of the sample with very high temporal resolution. For controllably approaching a metallized tip to fluorescence molecules, atomic force microscopy (AFM) is used. It permits accurate height profiling on the basis of force measurements between a sharp probe tip and a surface and thus allows to accurately position it relative to a molecule. All three techniques are introduced in chapter 3, along with a short introduction to theoretical approaches for the evaluation of single-molecule data.

Chapter 4 is devoted to the study of a polymeric host/guest system, in which molecular interactions between hosts and guests give rise to structural changes upon tensile deformation. Short, fluorescent rigid-rod molecules are blended with long-chain, nonfluorescent polyethylene molecules. After stretching, SCOM reveals diffraction-limited isolated spots. Fluorescence time traces acquired on fluorescent spots indicate that the fluorescent features are isolated chromophores or clusters of few chromophores. Quantitative analysis of the cluster size distributions as a function of the degree of stretching reveals that initially present phase-separated domains are broken up into small clusters of guest molecules. At the same time, the increasing

interaction of guest and host molecules forces the fluorescent guest molecules to adopt the preferential orientation of the matrix, as evidenced by the increasingly polarized fluorescence emission.

In chapter 5, the statistical analysis of bioassays at the level of single molecules is investigated exploiting superresolution optical techniques. Dual-colour wide-field microscopy on fluorescence-labelled ligand and receptor molecules, which are immobilized on a substrate, reveals intermolecular distances with subdiffraction-limited accuracy. On the basis of fundamental statistical arguments, a probability for specific binding, as opposed to incidental vicinity, can be assigned to each observed pair of ligand and receptor molecules. For groups of events, a complete statistical characterization of the experimental outcome is given in the form of a probability distribution. To permit an objective comparison between different experiments, a reliability parameter is defined. It is seen that the observation of few events is sufficient to conclude with highest statistical confidence that specific binding has occurred.

For the experiment described in chapter 8, realtime measurement of the excited state lifetime of a single molecule is required. Time-correlated single-photon counting (TCSPC) in its commonly employed form relies on offline fitting of measured data and is therefore hard to synchronize with an experiment. Chapter 6 outlines the design and implementation of an online lifetime-measurement device. The circuit described does not require any type of memory and is implemented easily. At low fluorescence count rates, its performance is better than that of commonly used online lifetime measurement schemes, and only slightly worse than the performance of a digital averaging circuit. To demonstrate the applicability of the scheme, fluorescence lifetime imaging with a SCOM was performed, indicating that on a single-molecule sample, lifetime differences due to the orientation of the molecular emission dipoles can be clearly resolved.

In contrast to chapters 4 and 5, where interactions of molecules are governed by statistics, chapter 8 deals with the controlled perturbation of molecules by metallic objects. By means of a sample-scanning SCOM, molecules embedded in a thin polymeric film can be located on a sample and positioned within the confocal volume for



---

continuous monitoring of their fluorescence intensity and lifetime. An independently controllable AFM allows for approaching a metallized scanning probe microscopy tip to the molecule under study. The presence of metallic surfaces gives rise to an altered boundary condition for the electric field emitted by a molecule and is thus manifested in its fluorescence intensity and -lifetime. For an understanding of the fluorescence dynamics of molecules in close proximity to metallic surfaces, an analytical approach to the derivation of the fluorescence lifetime in planar multilayered geometries is outlined in chapter 7. Experimentally, the fluorescence intensity and lifetime are mapped for variable relative tip-molecule distances. For the fluorescence intensity, a sharply localized decrease superimposed onto an interference-type fringe pattern is observed. The latter is presumably caused by scattering of excitation light on the AFM tip, while the sharp decrease is of near-field origin. The fluorescence lifetime map does not exhibit a fringe pattern, but shows a dip of dimensions identical with the near-field feature seen in the intensity map, indicating that the presence of the metallic tip provides a very effective pathway for radiationless dissipation of excitation energy to the metallic tip. This interpretation is further corroborated by the simultaneously lowered count rate in the intensity map, which is interpreted as an increase of the nonradiative decay rate in the rate-equation model of chapter 2.



## 2. Fundamentals of Single-Molecule Spectroscopy

In this chapter, fundamental prerequisites for observing the fluorescence signal of individual molecules are introduced. The photophysical behavior of single molecules at room temperature is derived from a rate-equation model for a three-level system. Using these results and simple signal-to-noise ratio considerations, it will be discussed how the experimental conditions for detecting single molecules can be optimized. Finally, it will be discussed how single-molecule experiments can unveil details of molecular behavior, which are not accessible with conventional ensemble measurements

## 2.1 Photophysics of a Single Molecule

Fig. 2.1 depicts the simplified energy level scheme of a dye molecule. The molecule can be excited from its ground state ( $S_0$ ) into its first excited state ( $S_1$ ) with a rate  $k_{12}$ , which is proportional both to the absorption cross section  $\sigma$  of the molecule and to the incident excitation intensity  $I$  as  $k_{12} = \sigma I$ . Decay from the excited state can occur either radiatively with a rate constant  $k_r$ , or nonradiatively with a rate constant  $k_{nr}$ . The total transition rate from the first electronically excited state to the ground state, which is inversely proportional to the fluorescence lifetime  $\tau$ , is thus given by:  $k_{21} = \tau^{-1} = k_r + k_{nr}$ . Intersystem crossing (ISC) to the triplet state (T) occurs with a rate constant  $k_{ISC}$ . Relaxation from the triplet state back to the ground state takes place with a rate  $k_T \ll k_{21}$ . The lifetime of the triplet state  $k_T^{-1}$  can be on the order of ms. At room temperature, the dynamical behavior of this

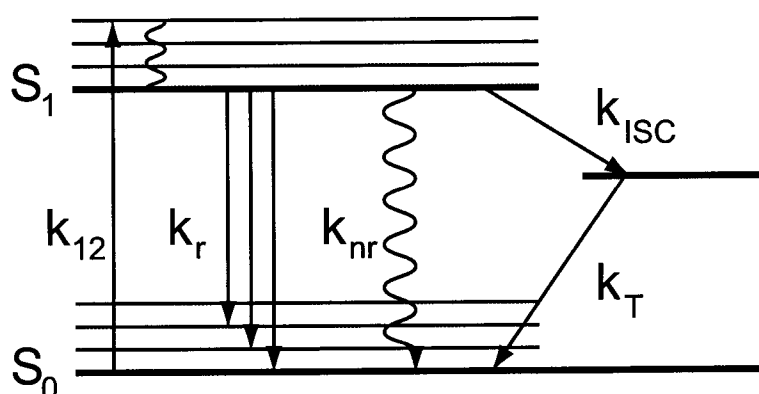


Figure 2.1: Jablonski diagram of a dye molecule with the electronic ground and first excited state  $S_0$  and  $S_1$  with their vibronic states and the triplet state  $T$ .  $k_{12}$  denotes the rate of excitation,  $k_r$  and  $k_{nr}$  are the rates for radiative and nonradiative relaxation, respectively. Intersystem crossing occurs with a rate  $k_{ISC}$ , relaxation from the triplet state back to the ground state with the rate  $k_T$ .

three level system can be described by a set of rate equations:

$$\begin{aligned}
 \frac{dp_1}{dt} &= -k_{12}p_1 + k_{21}p_2 + k_T p_3 \\
 \frac{dp_2}{dt} &= +k_{12}p_1 - k_{21}p_2 - k_{ISC}p_2 \\
 \frac{dp_3}{dt} &= +k_{ISC}p_2 - k_T p_3
 \end{aligned}
 \tag{2.1}$$

Taking the normalization condition  $p_1 + p_2 + p_3 = 1$  into account and solving equations 2.1 for the stationary case,  $\frac{dp_i}{dt} = 0$ ,  $i = 1, 2, 3$ , the dependence of the occupation probabilities  $p_1$ ,  $p_2$  and  $p_3$  on the excitation intensity is found. The quantity of interest for single-molecule fluorescence experiments is  $R = k_r p_2$ , the fluorescence emission rate. Substitution of  $p_2(I)$  into the expression for  $R$ , leads to:

$$R(I) = \frac{R(\infty)}{1 + \frac{I_S}{I}}. \quad (2.2)$$

Equation 2.2 reflects hyperbolic saturation behavior as a function of excitation intensity with two parameters  $R(\infty)$  and  $I_S$ , where  $R(\infty) = \frac{k_r}{1 + (k_{ISC}/k_T)}$ , and  $I_S = \frac{R(\infty)}{\sigma} (1 + \frac{k_{ISC}}{k_r})$ .  $R(\infty)$  is the saturation count rate, i.e. the number of photons per second emitted by the molecule at infinitely strong illumination. In order to obtain fluorescence signals of appreciable magnitude, also for moderate excitation intensity,  $R(\infty)$  should be as large as possible. The expression for  $R(\infty)$  indicates, how this can be achieved:

1. Ideally, molecules with large  $k_r$ , i.e. large rates for radiative relaxation should be chosen.
2. The fluorescence quantum yield  $\phi_F = \frac{k_r}{k_{21}}$  should be as close to unity as possible.  $\phi_F$  signifies the relative contribution of  $k_r$  to  $k_{21}$ , the fraction of transition events from state (2) to state (1), which give rise to emission of photons.
3.  $\frac{k_{ISC}}{k_T}$  should be as small as possible, which leads to avoiding triplet shelving, i.e. high probabilities for trapping of the molecule in the triplet state. This requirement is satisfied by choosing molecules with low  $k_{ISC}$ , i.e. minimizing the number of intersystem crossing events. On the other hand, large values of  $k_T$  give rise to fast return of the molecule to the ground state, reducing the average residence time of the molecule in the triplet state.

In order to facilitate excitation, the saturation intensity  $I_S$ , i.e. the intensity required to achieve half of  $R(\infty)$ , should be as small as possible. In addition to the previously mentioned requirements, this means that the absorption cross section of the molecule should be as large as possible. These requirements are often met by standard laser

dyes. In order to find typical values for  $R(\infty)$  and  $I_S$ , the parameters for a typical dye (terrylene) [12] are inserted into the above expressions:

$$\phi_F \approx 1, \quad k_T^{-1} \approx k_{21}^{-1} = 5 \text{ ns}, \quad \sigma = 10^{-9} \text{ } \mu\text{m}^2$$

$$k_{\text{ISC}}^{-1} = 2 \text{ } \mu\text{s}, \quad k_T^{-1} = 10 \text{ } \mu\text{s}$$

yielding  $R(\infty) \approx 3.3 * 10^7 \text{ counts s}^{-1}$  and  $I_S = 11 \text{ } \mu\text{W}/\mu\text{m}^2$ .

Assuming a total detection efficiency of 10 % for a typical confocal setup (chapter 3.1.2) with an objective of numerical aperture 1.4, this means that a maximum rate of  $\approx 3.3 * 10^6 \text{ counts s}^{-1}$  can be detected from a good fluorophore. However, at room temperature, photodestruction of the molecule, e.g. due to chemical reactions with singlet oxygen, places an upper limit on the total number of detectable photons.

In conclusion, these considerations show that at moderate excitation intensity levels, typical fluorescence molecules emit photons at a rate, which is easily detectable using single-photon sensitive detectors, such as avalanche photo diodes (APDs) or photomultiplier tubes (PMTs).

## 2.2 Selectively Addressing Single Molecules

Although in principle a single molecule can be easily detected according to section 2.1, the ability to selectively excite single molecules is another vital ingredient to single-molecule detection and -spectroscopy.

Historically, the first fluorescence experiments on single molecules were spectroscopic studies carried out at cryogenic temperatures using narrowband tunable lasers [5, 13–15]. In these studies the observation of single molecules was achieved in transparent molecular crystals doped with fluorescent impurities at low concentrations. Although many molecules are physically present in the excitation volume, only molecules in resonance with the narrowband laser are excited. Consequently, the effective density of molecules is strongly reduced, such that at the wings of the inhomogeneous absorption band, excitation spectra of isolated zero-phonon lines of

single molecules become observable. When tuning the laser to the wings of the inhomogeneous absorption band, fluorescent molecules which are embedded in a matrix can thus be addressed selectively.

In contrast, at ambient temperature, where the spectra of individual molecules are very broad due to the occupation of vibronic levels, accurate selection of molecules via the laser frequency is no longer possible. It is therefore necessary to reduce the spatial extent of the excitation volume and to decrease the concentration. This can be done by strong lateral confinement of the excitation light, as in near-field microscopy [8], by confocal microscopy [16, 17], or by z-confinement of excitation light, as in total internal reflection (TIR) schemes [18, 19], or by using thin samples.

## 2.3 Signal-to-Noise Ratio Considerations

When choosing experimental conditions, which allow for reducing the number of observed molecules to one, the signal-to-noise ratio for single-molecule observations requires careful consideration [15]. The signal-to-noise ratio SNR reads as:

$$SNR = \frac{DR(I)\Delta T}{\sqrt{DR(I)\Delta T + C_b I \Delta T + N_d \Delta T}} \quad (2.3)$$

where  $\Delta T$  is the integration time.  $I$  is the excitation intensity,  $C_b$  is the background count rate per incident illumination intensity, and  $N_d$  is the dark-count rate of the detector.  $R(I)$  is the emission rate of the molecule at the given excitation intensity, as given by eq. 2.2 in section 2.1. The factor  $D = \eta_q \eta_o$  accounts for the overall detection efficiency of the setup, where  $\eta_o$  is the optical collection efficiency, taking into account the numerical aperture of the objective and the loss of fluorescence due to filter elements, and  $\eta_q$  is the quantum efficiency of the detector.

The numerator of the above expression is equivalent to the fluorescence signal collected from an individual dye molecule, according to equation 2.2, while the denominator specifies the shot-noise, which is proportional to the square root of the *total* collected signal. In addition to the single-molecule signal, it contains two more

terms:  $C_b I \Delta T$  is the signal due to background fluorescence and scattering,  $N_d \Delta T$  is the dark-count signal accumulated within the integration time  $\Delta T$ .

Inspection of equation 2.3 shows the main requirements that have to be fulfilled for single-molecule spectroscopy (SMS): The detector should not only have a high quantum efficiency  $\eta_q$ , but also a low dark-count signal. Secondly, sample and filters have to be chosen such that the background signal is as low as possible. It should be noted that the effects of the latter can become particularly disadvantageous at higher excitation intensities, when saturation of the single-molecule fluorescence sets in. As  $I$  goes beyond  $I_S$ ,  $R(I)$  reaches  $R(\infty)$ , while the background signal still increases linearly with intensity. This effect, which leads to a decrease of the signal-to-noise ratio, is illustrated in Fig. 2.2.

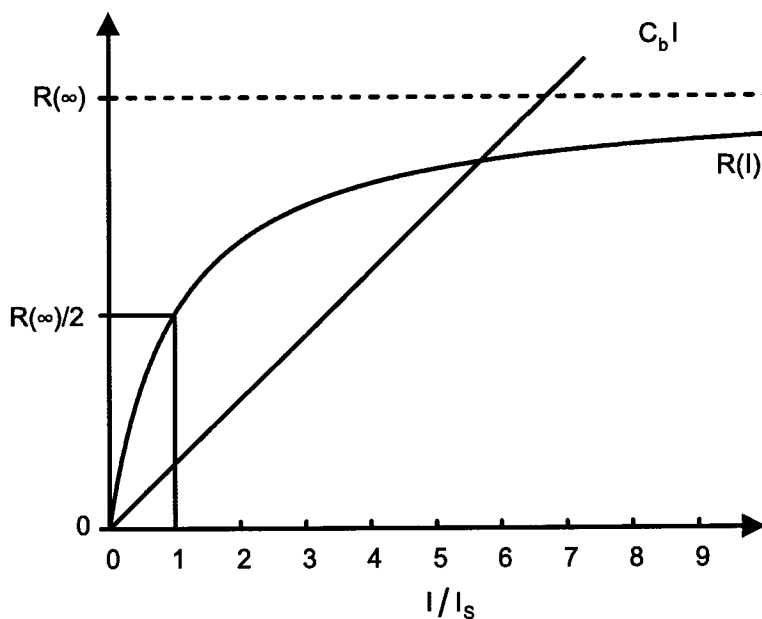


Figure 2.2: Comparison between the saturation behavior of a molecule  $R(I)$  and the linear increase of background fluorescence  $C_b I$  with illumination intensity



## 2.4 Specific Advantages of Single-Molecule Observations

Experiments on single molecules provide information, which cannot be obtained in ensemble experiments. While conventional ensemble experiments only allow for accessing averaged physical quantities  $\langle X \rangle$ , single-molecule experiments permit to determine *distributions* of physical quantities  $X$ . These distributions arise from two types of heterogeneities encountered within an ensemble:

1. Static heterogeneities: Molecules which differ structurally or which are influenced by their surroundings in a particular way, are characterized by different time-averages of physical observables
2. Dynamic heterogeneities: Although structurally identical, and being statically homogeneous, molecules show different temporal evolution of physical observables

When reducing the size of the ensemble under observation to one, i.e. a single molecule, heterogeneous behaviour is directly observable, providing direct insight into processes at the molecular level. In the following, this is exemplified by two systems:

Single dye molecules are a conceptually very simple system for illustration of the differences between static and dynamic heterogeneities. A three-level system, as depicted in Fig. 2.1, is fully characterized by a set of rate-constants for transitions between individual states of the molecules. The time-averaged fluorescence intensity of a molecule is defined unambiguously by the rate constants. A statically heterogeneous ensemble is thus constituted by subsets of molecules with differing rate constants. With single-molecule spectroscopy, transition rates can be determined for each individual molecule, and subclasses of molecules identified. In spite of being statically homogeneous, the members of such a subclass are still dynamically heterogeneous, i.e. their fluorescence time trajectories evolve differently. Although it is possible to synchronize an ensemble, e.g. by simultaneously exciting molecules, which were initially in the ground state, coherent behavior usually persists only for

very limited time. Single-molecule observations allow for analysis of both types of heterogeneity: Individual transitions between quantum states of the molecules (such as intersystem crossing with the associated dark period), as well as time-averaged observables can be measured. In addition, the observation of single molecules permits to follow the temporal evolution of an individual quantum system.

In biology, it is often of interest to study the functionality of a particular class of molecules. An example, where SMS was used to gain insight into heterogeneities of biological systems, is enzymatics [20]. A particular type of enzyme, which converts a nonfluorescent substrate into a fluorescent product, was monitored with confocal microscopy. Recording of fluorescence time trajectories of individual enzyme molecules revealed individual turnovers of the molecule as well as distributions of residence times in individual functional states. Analysis of the data in the frame of a rate-equation model for transitions between individual states allows to extract rate constants for the enzymes on a one-by-one basis. Consequently, performance differences between molecules and the reasons for such differences (trapping in certain states) can be found. With these results, different mutants of enzyme molecules could be identified and sequenced genetically. Such possibilities, which are unique to single-molecule techniques, permit systematic studies of structure-function relationships, which could provide fundamentally new insights into the functioning of enzymatically active sites.

For the studies performed in this thesis, the ability of single-molecule to reveal static and dynamic heterogeneities, is of essential importance. In chapter 4, distributions of cluster sizes are measured, providing information about static disorder in polymeric materials. Chapter 5 takes advantage of the high spatial accuracy achievable with optical microscopy in order to categorize pairs of molecules as belonging to two distinct ensembles: Those that are physically bound to each other, and those that are bound to the substrate at random. The work discussed in chapter 8, relies on measuring the dynamic near-field optical response of a single molecule to a controllable external perturbation.

In all three studies, single-molecule microscopy serves as a tool for the observation of heterogeneous single-molecule behaviour in complex surroundings.

### 3. Techniques and Concepts

In this chapter, fundamental aspects of both, the experimental techniques and the data analysis methods used in this thesis will be outlined. An introduction to the techniques of wide-field microscopy and scanning confocal optical microscopy (SCOM) will be given along with a discussion of their respective advantages and drawbacks. The basic principle of atomic force microscopy (AFM) is outlined, as far as required for the understanding of chapter 8. Brief mention will be made of statistical aspects of position, intensity and lifetime measurements.

## 3.1 Microscopy Techniques

### 3.1.1 Wide-Field Microscopy

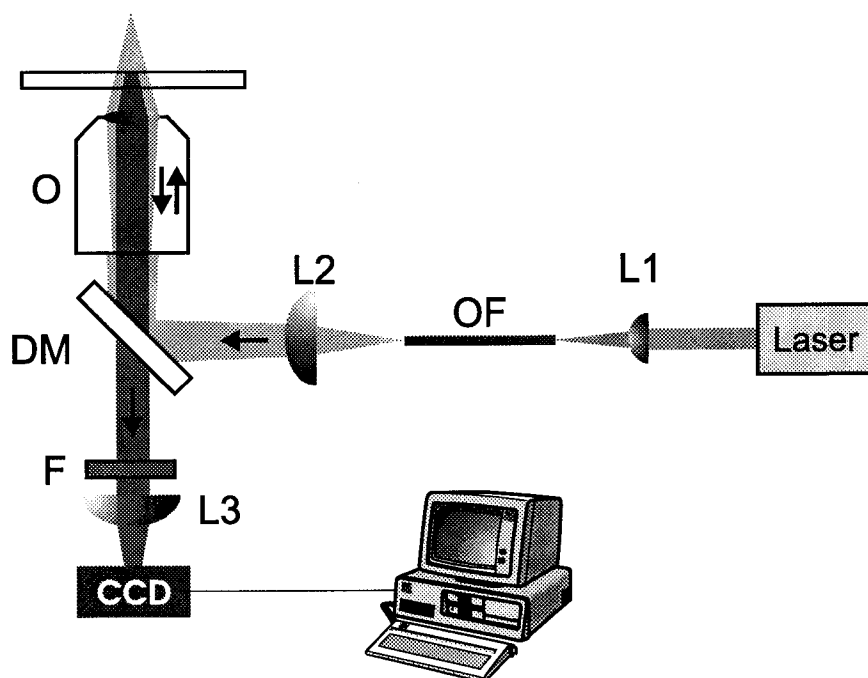


Figure 3.1: Setup for wide-field microscopy. L1, L2, L3: lenses; OF: optical fiber, DM: dichroic mirror, O: objective, CCD: charge-coupled device, F: cut-off filter

Fig. 3.1 shows a typical wide-field epifluorescence microscopy setup. For spatial filtering of the beam profile, the laser light is coupled into a single-mode optical fiber via lens L1, and outcoupled by lens L2. To achieve an extended illumination spot on the sample, L2 is positioned such that the illumination beam is slightly divergent at the back aperture of the objective O. Fluorescence is collected by the same objective, filtered by the dichroic mirror DM and the cut-off filter F and imaged onto the charge-coupled device (CCD) camera for computer-controlled image acquisition. On the CCD chip, incident fluorescence photons generate photoelectrons in an array of pixels. During the exposure time, charge is accumulated on each of these pixels. In the readout process, sequential measurement of the charge on each of the pixels allows to spatially map the number of fluorescence photons collected by the chip. The inherent advantage of imaging many molecules in parallel by CCD chips is

afforded by two drawbacks: (i) information about the arrival time of photons within the integration time is lost, and (ii), the readout process is rather slow, which ultimately limits the maximum rate of image acquisition.

A specific property of wide-field microscopy with regard to the choice of samples is that it collects all fluorescence, irrespective of its point of origin on the optical axis. When imaging thick samples, very large sample volumes are illuminated. Although only objects in the focal plane produce sharp images on the camera, light emitted by out-of-focus objects is also collected, leading to an increase of background signal and shot-noise. In order to avoid this problem, it is necessary to use thin films or membranes as samples, or using total internal reflection illumination, when studying single molecules by wide-field microscopy.

### 3.1.2 Scanning Confocal Optical Microscopy (SCOM)

Fig. 3.2 shows a typical scanning confocal fluorescence microscopy setup for polarization-resolved imaging. Spatial filtering of the laser beam profile is achieved by coupling the light into a single-mode optical fiber (OF) via lens L1. L2 is used for outcoupling of the light, resulting in a collimated beam. Subsequent to reflection on the dichroic mirror DM, the light is focused to a diffraction-limited spot on the sample by the objective O. Fluorescence is collected by the same objective and filtered from excitation light by DM and the cut-off filter F. For simultaneous acquisition of two polarization-resolved images, the fluorescence light is divided by a polarizing beamsplitter (PBS) prior to detection on two single-photon counting avalanche diodes (SPADs). Scanning of the sample with a three-axis scanner (S) allows for pixel-wise acquisition of the fluorescence signal and image buildup on a computer. In contrast to wide-field microscopy, where a CCD chip is used as a detector of large lateral extension, SPADs have a very small photosensitive area, and therefore can act as point detectors. In confocal geometry, which is illustrated in Fig. 3.3, the alignment is such that the excitation volume is imaged onto a pinhole in front of the detector. Signals emitted by objects out of the focal plane or from points, which are laterally displaced with respect to the focal volume, are not properly imaged onto the detector pinhole, and are therefore strongly suppressed. The selective de-

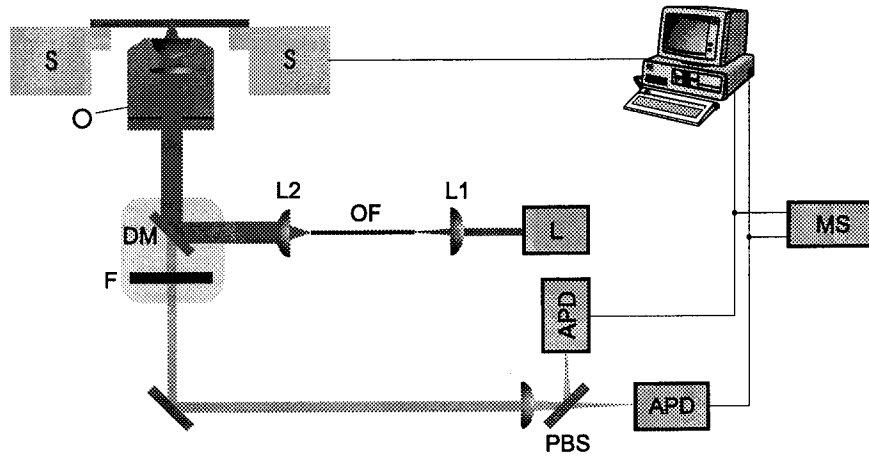


Figure 3.2: Setup for dual-polarization scanning confocal optical microscopy. L: laser; L1, L2: lenses; OF: optical fiber; DM: dichroic mirror; O: objective; S: xyz-scanner; F: cutoff filter; PBS: polarizing beamsplitter; APD: avalanche photodiode; MS: multichannel scaler

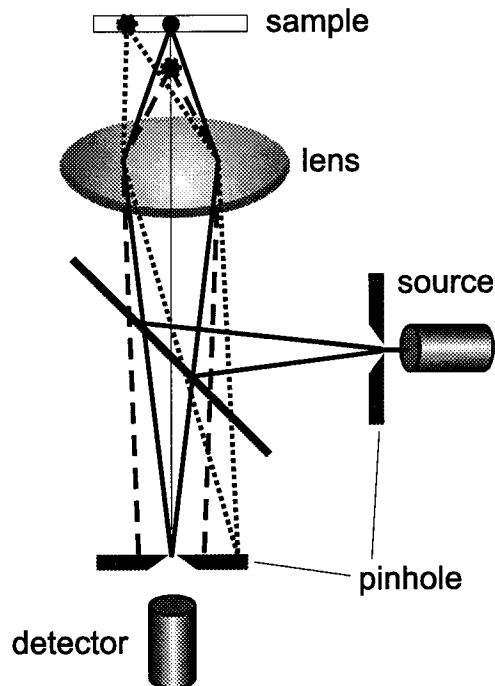


Figure 3.3: Background suppression in SCOM. The excitation volume is imaged onto the small photosensitive area of the detector, which acts as a pinhole. Objects out of the focal plane are imaged in front of or behind the pinhole (dashed line), and thus strongly suppressed. Laterally displaced objects (dotted line) are imaged beside the pinhole, also resulting in signal suppression.

tection of fluorescence only from the focal plane allows for optical slicing, i.e. the acquisition of images at well-defined z-positions. Sets of optical slices recorded for different positions of the focal plane can be combined to obtain three-dimensional reconstructions of thick samples. A further advantage of the method is the high time-resolution for single-photon counting. The arrival time of each individual photon can be measured with an accuracy of  $\approx 300$  ps on individual pixels. However, image acquisition requires a scanning process, and SCOM is therefore inherently serial, setting limits on the acquisition time for a single image. In comparison to wide-field setups, the acquisition of a complete image is much slower in SCOM.

### Illumination Point-Spread Function for SCOM

In chapter 3.2.1, it is discussed, how statistical analysis of fluorescence intensities can be used to measure cluster size distributions. In order to extract intensity information from SCOM image data, individual subdiffraction-limited fluorescent features have to be fit with the point-response of the microscope. Provided that the detector pinhole is chosen large enough to collect the entire fluorescence emitted within the confocal volume, a subdiffraction-limited object maps out the illumination intensity distribution in the focus. The latter is mostly referred to as illumination point-spread function (IPSF). In this section, its shape will be derived in paraxial approximation, and it will be shown that Gaussian functions reproduce the central maximum of the IPSF very well. The shape of the IPSF can be derived easily from Huygens' principle. Figure 3.4 (a) shows the geometry used for the derivation. A plane wave is incident onto a lens, which is essentially an aperture of radius  $2a$ . According to Huygens, a spherical wave of the form

$$E_0 \frac{\exp(ikR)}{R}, \quad (3.1)$$

originates from each point of the aperture, where  $R$  is the distance from the point of origin in the aperture plane to a point in the image plane, which is at distance  $d$ . In figure 3.4 (b), the choice of coordinates is shown. Both, in the aperture plane and the image plane, polar coordinates are used;  $\rho$  and  $\delta$  for the aperture plane,  $r$  and  $\varphi$  for the image plane. Due to rotational symmetry,  $\varphi$  can be set

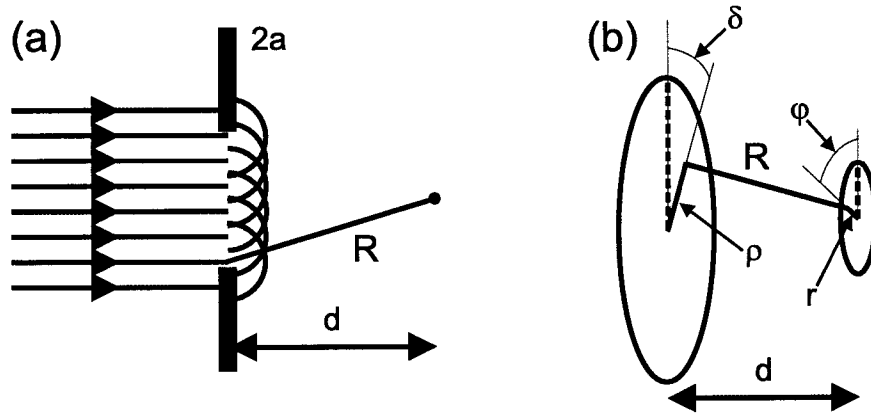


Figure 3.4: (a) Diffraction of a plane wave at a circular aperture according to Huygen's principle: A spherical wave originates from each point of the aperture of diameter  $2a$ , the diffraction pattern at a distance  $d$  is to be calculated.  $R$  is the distance of an individual point on the aperture to the respective point in the image plane (b) Choice of coordinates. Polar coordinates are used both in the aperture plane  $(\rho, \delta)$  and the image plane  $(r, \varphi)$

to zero, and the expression for  $R$  becomes:  $R = \sqrt{d^2 + r^2 + \rho^2 - 2\rho r \cos\delta}$ . For not too large numerical apertures, the following Taylor-approximation can be used:  $\sqrt{1 + \epsilon} \approx 1 + \frac{\epsilon}{2}$ . Neglecting the  $\rho^2$  term and integrating over all points in the aperture plane, the electric field in the image plane is obtained:

$$E(r) \propto E_0 \int_0^a \int_0^{2\pi} \frac{\exp\left(\frac{ikr\rho}{d} \cos\delta\right)}{d} \rho \, d\rho \, d\delta, \quad (3.2)$$

where the small variations of  $R$  have been neglected in the denominator of the integrand. The result for the electric field is given by:

$$E(r) \propto \frac{J_1\left(\frac{kra}{d}\right)}{\frac{kra}{d}} \quad (3.3)$$

Consequently, the intensity point-spread function is given by:

$$I(r) \propto \left( \frac{J_1\left(\frac{kra}{d}\right)}{\frac{kra}{d}} \right)^2 \quad (3.4)$$



This type of function is called Airy-function. An important fact with regard to image analysis is that this function can be fit very well with Gaussian distributions, as seen in fig. 3.5.

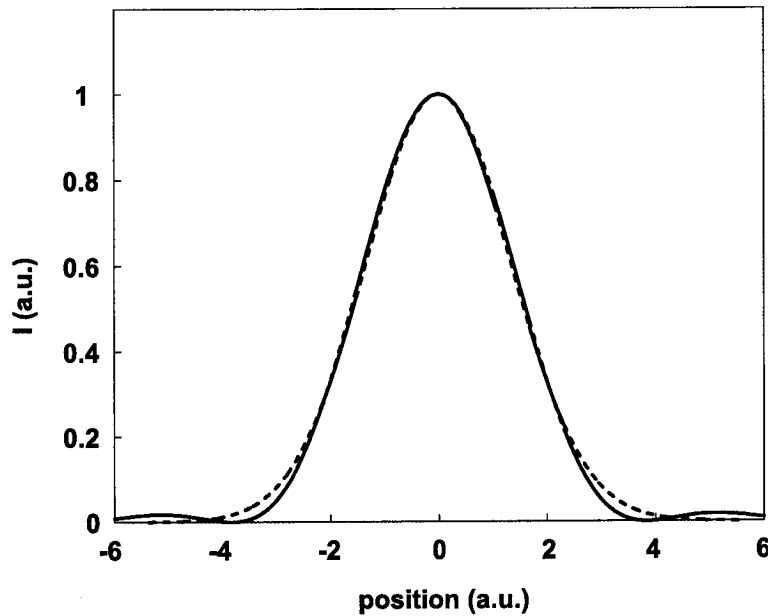


Figure 3.5: Comparison of an Airy-function (solid line) with a Gaussian of equal width. The central maximum is reproduced well, the relative intensity in the side-fringes is comparably low.

### 3.1.3 Atomic Force Microscopy

In AFM [4], the topography of a sample is measured, based on the detection of a force between a tip and the sample. AFM probes are mostly designed as flexible levers with sharp tip structures at their end, as illustrated in Fig. 3.7. Force sensing is achieved by measuring the deflection of the lever, as the tip comes into close contact with the sample. For accurate detection of the deflection, a laser is reflected off the backside of the probe lever and imaged onto a four-quadrant detector (left side of Fig. 3.7). For a laser beam, which is centered on the detector, each quadrant will receive the same intensity. When the lever is either bent or subject to torsional stress, the intensity will shift to the upper quadrants or the left/right quadrants, respectively. Denoting the intensities measured on quadrants 1, 2, 3 and 4 as  $I_1, I_2, I_3$

and  $I_4$ , it is seen that the deflection  $\Delta z$  is obtained as  $\Delta z \propto (I_3 + I_4) - (I_1 + I_2)$ , and that torsional deflection is given by  $\Delta\varphi \propto (I_1 + I_4) - (I_2 + I_3)$ . On the basis of this information about lever deflection, topographic images of the surface can be acquired. This is realized by coarsely approaching the tip to the sample by means of a stepper motor, and finally making contact with a piezo actuator until a preset value for the lever deflection is achieved. After the approach, tip-scanning in the x-y plane is started. If the tip were scanned at constant height, it would bend further, when encountering elevated parts of the sample, and thus exert more force. To keep tip-sample forces low and avoid destruction of the sample, a piezo actuator approaches or retracts the tip such that the preset lever deflection remains constant. When plotting the piezo extension in z as a function of the lateral position on the sample, a map of the surface topography is obtained. Displaying  $\Delta\varphi$  as a function of lateral position results in a friction force map of the sample.

The distance-dependent tip-sample force is derived from an interaction potential. A qualitative description of the latter is given e.g. by Lennard-Jones-type potentials. The most commonly discussed 6-12 Lennard-Jones potential, is depicted in figure 3.6. At very small distances, strongly repulsive interactions between the atoms on

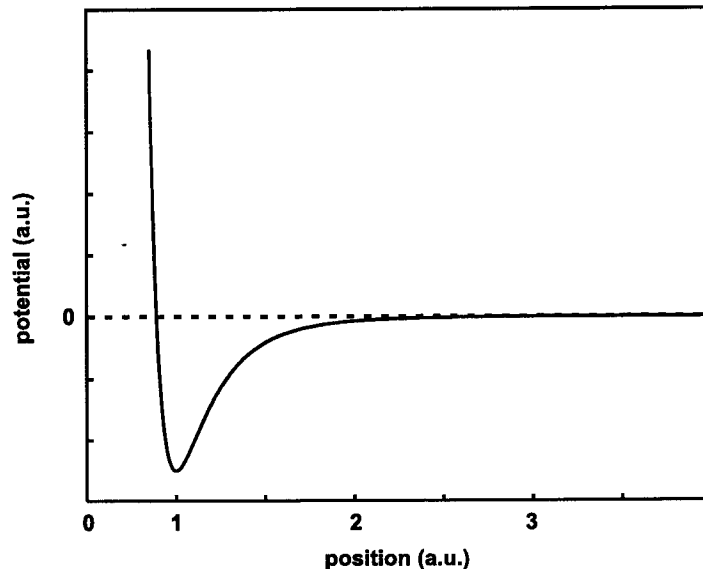


Figure 3.6: Distance dependence of the tip-sample interaction potential, as described by a Lennard-Jones potential. At small distances, repulsive interactions between tip and sample set in, while attractive forces dominate at intermediate distances.

the tip apex and the sample atoms prevail, whereas at intermediate distances, van der Waals attraction and electrostatic interactions give rise to attractive forces. For detecting interaction forces  $f(z) = -\frac{\partial V}{\partial z}$ , there are two mainly employed modes: (a) Measurement of static forces due to repulsive interaction, commonly called *contact mode* and (b) Measuring the damping of an oscillating cantilever due to repulsive forces, commonly called *noncontact mode*. In the following, only (a) will be discussed, since (b) was not employed for the present work.

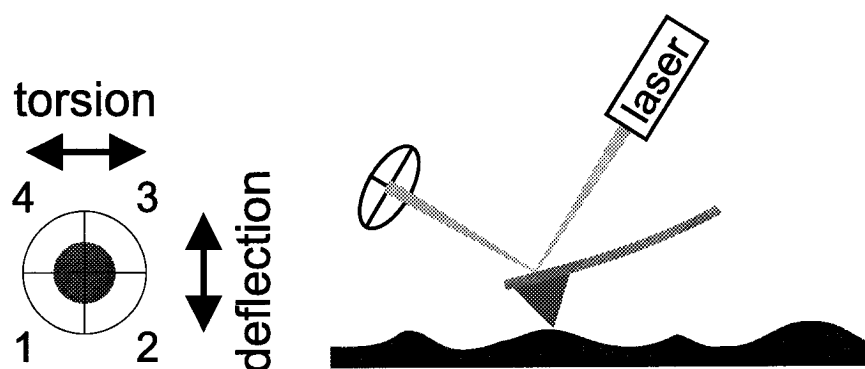


Figure 3.7: Detection of lever deflection in atomic force microscopy. The four quadrant detector shown on the left measures intensity differences between the upper and lower or left and right half, respectively, allowing to deduce  $z$ -deflection and torsional deflection.

## 3.2 Data Analysis Techniques

### 3.2.1 Stoichiometric Quantitation of Cluster Sizes

In chemistry and biology it is often of interest to determine the size of molecular aggregates with stoichiometric accuracy. However, the length scales of most systems defy direct visualization with optical techniques. Here, the accurate measurement of fluorescence intensities with single-molecule techniques can be used to gain size information about structures smaller than the resolution limit [21].

On an ensemble of well-defined isolated chromophores, it is possible to measure distributions of fluorescence intensities, and to determine the expectation value for the

fluorescence intensity  $I_1$  of a single chromophore. If molecules of the same type are employed as a marker, aggregation can be monitored by observation of fluorescence intensities [21]. Assuming that a number  $n$  of identical marker molecules is contained in a volume significantly smaller than the detection volume and that these molecules do not perturb each other strongly (e.g. by nonradiative energy transfer or electron transfer), the expectation value of their total fluorescence intensity is  $I = nI_1$ . It is thus possible to obtain an estimate of  $n$  by comparison of the measured fluorescence intensity with the unitary value for one molecule:  $n = \frac{I}{I_1}$ .

Experimentally, the data is mostly acquired in the form of microscopy images, which exhibit fluorescent features due to isolated molecules or clusters of molecules. Their total signal strength is obtained by fitting the spatial intensity profile with the point-spread function (psf) of the microscope, which can be approximated well by a Gaussian, as shown in chapter 3.1.2. Fitting yields the spatial position  $(x, y)$  of the maximum as well as the integrated intensity  $I'$  of a feature, and the respective errors  $(\Delta x, \Delta y)$  and  $\Delta I$ . Assuming that the experimental errors obey a Gaussian distribution, the following probability density function (pdf) for the fluorescence intensity  $I$  of a single molecule can be estimated:

$$\rho(I) = \sqrt{\frac{1}{2\pi(\Delta I)^2}} \exp\left(-\frac{(I - I')^2}{2(\Delta I)^2}\right) \quad (3.5)$$

In a probabilistic sense, this pdf approximates the full description of all possible experimental outcomes of a *single* measurement.

The pdf for intensity measurements on an ensemble of isolated molecules is obtained by addition of pdfs of the form given in eq. 3.5 for each member of the ensemble and subsequent renormalization. Such a composite pdf specifies the probability density for measuring an intensity  $I$ , when selecting an arbitrary molecule out of the ensemble. For ensembles of many molecules, its shape is again well described by a sum of Gaussians. Hence, Fig. 3.8 (a), which would be measured for the observation of an ensemble of identical molecules, is a single Gaussian obtained by addition of many Gaussians with distributed center intensities. The maximum of the distribution is at the unitary fluorescence intensity  $I_1$ . For samples containing clusters of molecules with different stoichiometries, multiple-peaked distributions are

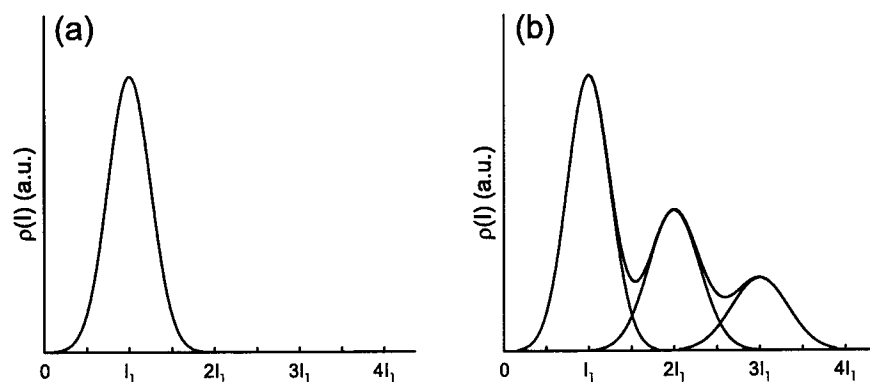


Figure 3.8: (a) Probability density function (pdf)  $\rho(I)$  for the case of an ensemble of identical isolated molecules. (b)  $\rho(I)$  for molecular clusters comprising 1,2 and 3 molecules with the unitary fluorescence intensity  $I_1$ . Due to shot-noise, the peaks become successively broader.

obtained, as exemplified in Fig. 3.8 (b) for the case of clusters consisting of 1,2 and 3 molecules. The probabilities of occurrence for clusters consisting of  $n$  molecules are given by the area under the  $n$ th peak. Shot noise causes broadening of the peaks proportional to  $\sqrt{n}$ , placing a limit on the countability of molecules: If  $\sigma_1$  is the uncertainty of intensity determination for one molecule, the uncertainty  $\sigma_n$  for the  $n$ th peak will be  $\sigma_n = \sigma_1\sqrt{n}$ , correspondingly [22]. It is obvious that stoichiometric accuracy is no longer possible, when  $\sigma_n$  exceeds the signal  $I_1$  of a single molecule. The upper limit for the cluster size, which can be identified unambiguously, is thus given by:  $N_{\max} = (I_1/\sigma_1)^2$ .

### 3.2.2 Superresolution Position Determination

Fitting of Gaussians to the point spread function of a microscope does not only yield the intensity, but also the position of a fluorescence molecule. For structural analysis using fluorescence microscopy, positional information is of importance. In computer-assisted fluorescence microscopy, images are acquired by sampling spatial intensity distributions at a discrete number of points. If *a priori*-information about the signal shape is available, fitting of the sampled signal can yield accurate information about amplitude and spatial position of the signal, even if the spacing of the sampling points is not significantly smaller than the spatial extension of the signal itself. In

optical microscopy, single molecules can be viewed as point-like emitters, which cause an image of the shape of the intensity point spread function (psf). As was shown in chapter 3.1.2, the psf is an Airy-function, which can be approximated very well by a Gaussian. For a noisy signal, fitting can only be performed in a least-squares sense, giving rise to uncertainties on parameter values. Fig. 3.9 shows a simulation of a signal of Gaussian shape. Within the errors for Poissonian counting statistics (indicated by the error bars), there are several choices of the center position, which are compatible with the error bars, as indicated by the grey bar. As is obvious from

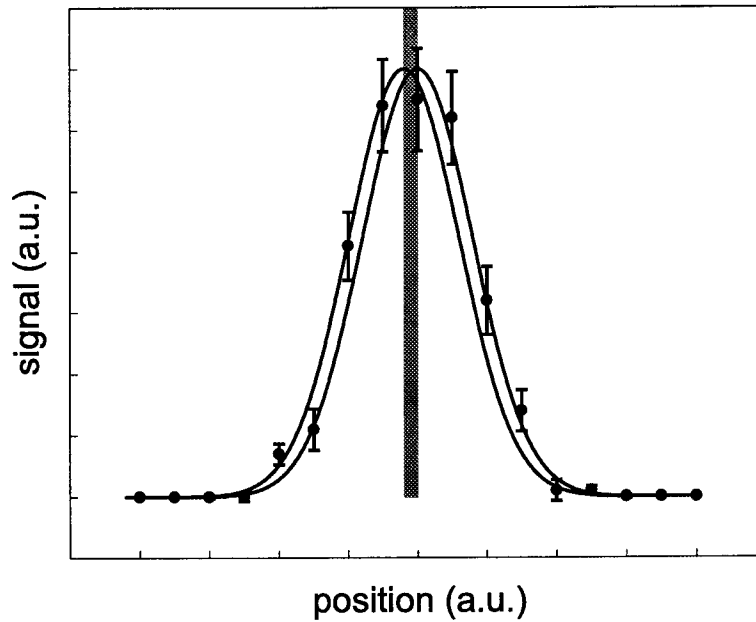


Figure 3.9: Simulation of a sampling process including shot-noise. Error bars indicate the uncertainty on measured intensities. The grey bar indicates the range of possible values for the center position of the Gaussian.

Fig. 3.9, the accuracy for locating the center position of the Gaussian is better than would be expected from the distance between sampling points, and the width of the Gaussian. For  $\chi^2$  fitting procedures and Gaussian signal shape  $R(S, \bar{x}_m, x) = S \exp(-\frac{(x-\bar{x}_m)^2}{2\Gamma^2})$ , the achievable positional precision can be derived analytically [23]:

$$\frac{x - \bar{x}_m}{\Gamma} \propto \frac{1}{S/\sigma_b} \sqrt{\frac{\Delta}{N_\Gamma}} \quad (3.6)$$

where  $\bar{x}_m$  is the center position of the fitted Gaussian,  $\Gamma$  denotes its width,  $S$  is its amplitude,  $\sigma_b$  the background noise level,  $\Delta = \chi^2 - \chi_{\min}^2$  is the deviation of  $\chi^2$  from its minimum value and  $N_\Gamma$  the number of sampling points in the distance  $\Gamma$ .

Equation 3.6 shows that there are two ways of improving positional accuracy: (i) The number of sampling points can be increased and (ii) the signal-to-noise ratio should be as high as possible. In the case of a wide-field single-molecule microscopy setup [24], where  $S/\sigma_b \approx 30$  and  $N_\Gamma \approx 3$ , a positional accuracy of about 30 nm was achieved, which is much smaller than the full width at half maximum of the intensity point spread function of 480 nm.

While this result does not mean any enhancement of resolution, significant advantages arise from the use of a dual-color microscopy setup. Fig. 3.10 shows two Gaussians in close vicinity, which could not be resolved in a monochromatic experiment. As a consequence of the added spectral selectivity, both Gaussians can be recorded separately, and the position of each can be determined with subwavelength precision. It is thus possible to determine their mutual position with very high accuracy. In the case of the abovementioned parameters,  $2 * 30 \text{ nm} \approx 60 \text{ nm}$  are possible for determining intermolecular distances. For colocalization studies, where the spatial vicinity of distinct molecules is of interest, the diffraction limit of conventional monochromatic experiments can thus be circumvented. In chapter 5, this approach will be applied to the study of oligonucleotide hybridization at the single-molecule level.

### 3.2.3 Determination of Single-Exponential Decay Rates by Averaging

In chapter 6, the implementation of a device for sensitive fluorescence lifetime measurements will be discussed. Commonly, so-called time-correlated single-photon counting (TCSPC) is used for determining fluorescence lifetimes. In TCSPC, fluorescence is excited by a pulsed laser-source and the time lags between excitation and emission of a fluorescence photon are measured for many excitation-emission cycles. Solving equation 2.1, it follows that the excitation-emission time lags obey

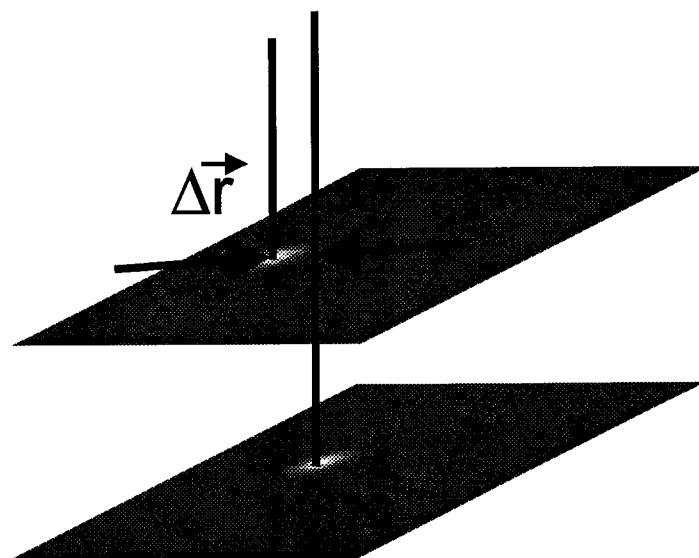


Figure 3.10: Distance measurement in a dual-colour experiment. Spectrally selective imaging of two distinct fluorescence molecules results in the upper and lower image, respectively. For each of the fluorescence spots, a positional *accuracy* beyond the diffraction limit is achieved, permitting superresolution measurements of the intermolecular distance.

a distribution function of the form

$$\rho(t_i) = \frac{1}{\tau} \exp\left(-\frac{t_i}{\tau}\right). \quad (3.7)$$

A series of  $N$  realizations  $\{t_1, t_2 \dots t_N\}$  of  $t$  would be measured, and binned into a histogram, as shown in Fig. 3.11. Fitting of the histogram allows to determine the  $1/e$ -value of the distribution, which is the fluorescence lifetime  $\tau$ .

For purely monoexponential decays, averaging over a number of excitation-emission time lags amounts to the same result, avoiding complicated fitting routines. This property is demonstrated in the following: To derive the probability density function  $\rho(T_n)$  for the realizations of sums  $T_N = \sum_{i=1}^N t_i$  over  $N$  photons, a theorem from statistics is used [22]: Assuming that  $\{Y_1, Y_2 \dots Y_N\}$  is a set of  $N$  realizations of a quantity, which obeys the distribution  $\rho(y_i) = \frac{1}{\lambda} \exp\left(-\frac{y_i}{\lambda}\right)$ , the sums  $X_N = \sum_{i=1}^N Y_i$  obey a Poisson distribution:

$$\rho(x_m) = \frac{(N\lambda)^m}{m!} \exp(-N\lambda m) \quad (3.8)$$



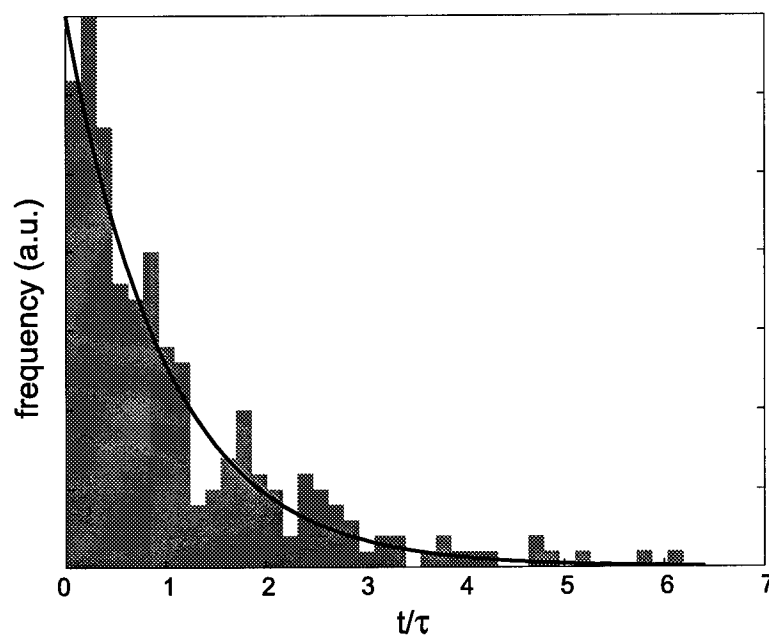


Figure 3.11: Representation of a simulated monoexponential excited state lifetime distribution as a histogram with an exponential fit (solid line)

Identifying  $\lambda$  in the above eq. 3.8 with  $\tau$  from eq. 3.7, it is seen that the expectation value of a sum over  $N$  excited state lifetimes is equal to  $N\tau$  and the average thus  $\frac{N\tau}{N} = \tau$ . Due to the properties of the Poisson distribution, the standard deviation is  $\tau\sqrt{N}$ . The relative standard deviation for determining  $\tau$  thus scales with  $N^{-1/2}$ . In chapter 6, considerations, which are in spirit similar to this result, will be used.



## 4. Tracing the Formation of a Molecular Polymer Blend

Photoluminescence microscopy of conjugated polymer molecules in a polyethylene host has been applied to monitor the transition of a phase-separated polymer blend into a molecular dispersion, induced by solid-state tensile deformation. Statistical analysis of conjugated polymer cluster sizes as a function of the degree of matrix deformation shows that phase-separated domains of conjugated polymer transform into smaller clusters and single molecules as the degree of matrix deformation increases. Concomitantly, the conjugated guest molecules tend to adopt the preferential orientation of the surrounding matrix. It is demonstrated that single-molecule detection can be readily extended and applied to probing molecular dispersion, orientation and morphology in polymer-polymer blends.

## 4.1 Introduction

Dispersions of macromolecules in a solid polymer matrix are of particular interest, because they can synergistically combine the properties of their components [25]. For example, blends of tailored properties of semiconducting conjugated polymers [26–29] and electrically inactive polymers may advantageously be used for applications in light-emitting devices [30], transistors [31], lasers [32], and other optical components [28]. The functionality of such materials critically depends on their structure at the molecular level. However, molecular mixing of two polymers in general, and of rigid-rod and flexible-coil macromolecules in particular, is usually inhibited by the unfavorably low entropy of mixing [25, 33, 34]. In special cases, this limitation can be overcome by the preparation of copolymers [35, 36] or by increasing the enthalpy of mixing, for example by introducing specific ion-ion or dipole-dipole interactions between the blend components [37, 38]. Significant efforts have previously also been devoted to shear-induced mixing of polymer blends [39]. In recent studies regarding the preparation of photoluminescent polarizers [40], it was surprisingly discovered that solid-state tensile deformation of initially phase-separated blends of a poly(2,5-dialkoxy-p-phenyleneethynylene) derivative (EHO-OPPE, [41] (Fig. 4.2) and ultra-high molecular weight polyethylene (UHMW-PE) results in a material in which the conjugated species exhibit bulk photoluminescent properties that indicate an apparent molecular dispersion of the rigid-rod conjugated polymer guest in the UHMW-PE host, although a true molecular dispersion might be thought of as unlikely for thermodynamic reasons [40].

### 4.1.1 Evidences for a Molecular Dispersion from Ensemble Experiments

The abovementioned evidence for molecular dispersion of the EHO-OPPE guest molecules in the UHMW-PE host is obtained from emission spectra of stretched and unstretched UHMW-PE/EHO-OPPE blends. Fig. 4.1 (a) shows that the luminescence spectra of pure EHO-OPPE and a pristine UHMW-PE/EHO-OPPE blend are almost identical, indicating a structural resemblance of EHO-OPPE in the pure

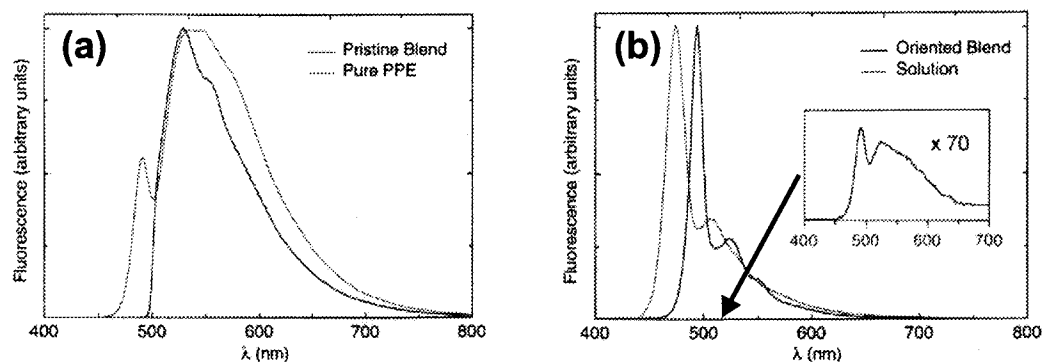


Figure 4.1: (a) Fluorescence spectra of pure EHO-OPPE and a pristine blend of UHMW-PE and EHO-OPPE. (b) Fluorescence spectra of dissolved EHO-OPPE and of a stretch-deformed UHMW-PE/EHO-OPPE blend. Taken from ref. [40]

state and in the blend with UHMW-PE. During stretching, the spectrum undergoes a striking change (Fig. 4.1): The broad, featureless spectrum is transformed into a narrow spectrum with clearly visible vibrational structure, which is very similar to the solution spectrum apart from a solvent shift. The spectral changes, strongly suggest, that initially phase-separated domains exist in the polymer blend, which are molecularly dispersed by the stretching process. In the following, single-molecule microscopy will be applied for direct visualization of this phenomenon.

## 4.2 Single-Molecule Studies

Single-molecule detection provides a handle to investigate the interaction of single photoluminescent species with their immediate environment. Measurements of absorption and emission dipole orientation [8, 42–48], and diffusional trajectories [19, 24], of individual absorbers have unveiled heterogeneous behavior at the level of sub-ensembles of molecular species. Such investigations therefore reflect the inhomogeneous nature of individual molecular environments and detailed - molecular-level - information on structural aspects of a chromophore-host composite can be provided. Single-molecule analysis provides direct and detailed insight into the structural rearrangement processes that occur in the above-mentioned EHO-OPPE/UHMW PE system. The spatial and orientational distributions as well as



Binary blend films and neat UHMW-PE reference samples of different deformation ratios  $\eta$  were investigated using standard fluorescence wide-field and fluorescence scanning confocal optical microscopy (as described in chapter 3.1.2) to image samples with a high and low concentration of conjugated polymer, respectively. The wide-field fluorescence microscope (Leica) was equipped with a UV lamp in combination with a suitable filter block (Leica, I2/3). The setup used for confocal imaging is of the type described in chapter 3.1.2. For excitation of EHO-OPPE, circularly polarized laser light at a wavelength of 488 nm from an Argon ion laser was used. The light was focused to a diffraction-limited spot by an immersion oil microscope objective (Zeiss, 1.4 NA,  $\infty$ ). The fluorescence light was collected by the same objective, filtered via a dichroic mirror and a cutoff filter ( $\sim 520$  nm) and directed towards a polarizing beamsplitter. The resulting orthogonal components of the fluorescence are detected by two SPADs. For acquisition of fluorescence time-traces, the SPADs were connected to a multichannel scaler.

## 4.4 Results and Discussion

Fig. 4.3 shows a  $100 \times 100 \mu\text{m}^2$  wide-field fluorescence image of a deformed ( $\eta = 80$ ) binary blend film containing 2% w/w EHO-OPPE. Highly fluorescent, stripe-like structures are observed with intermittent darker elongated domains oriented parallel to the stretching direction. The latter coincides with the preferential polarization of the fluorescence emission [40]. This observation strongly supports earlier photoluminescence, X-ray-, and electron diffraction experiments which indicate that the macroscopic tensile deformation leads to a "breaking up" and "smearing out" of the originally phase-separated EHO-OPPE clusters accompanied by an increasingly polarized fluorescence emission [40].

Fig. 4.4 shows typical polarized fluorescence images of a an unstretched ((a), (b)) and a stretched ((c), (d)) dilute ( $10^{-4}$  % w/w EHO-OPPE) binary blend film ( $\eta = 80$ ), respectively, recorded by detecting the polarization component parallel to the deformation direction. For the unstretched film (Fig. 4.4 (a) and (b)), neither features of diffraction limited size nor any preferential orientation are seen, consistent with the

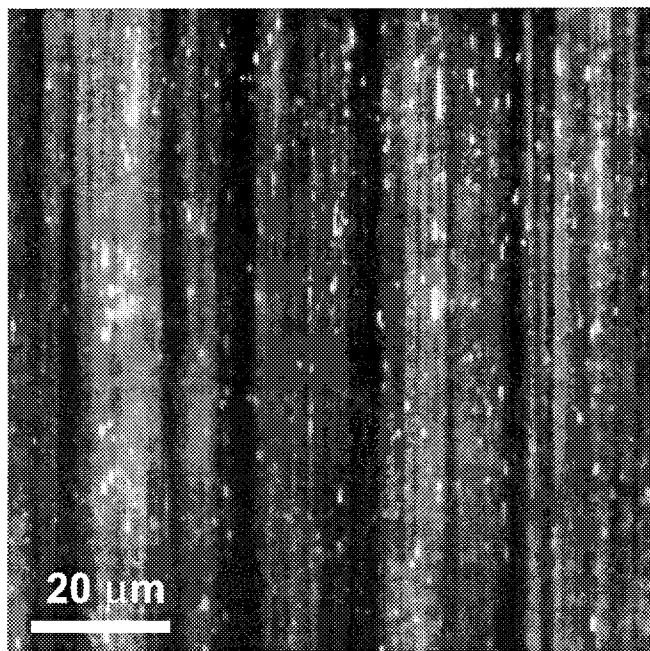


Figure 4.3: (Wide-field fluorescence image of a 2% w/w stretched ( $\lambda = 80$ ) film. Stretching direction is vertical. An inhomogeneous, stripe-like distribution of fluorescent polymer is seen. The regions of bright fluorescence appear elongated along the direction of stretching

presence of large, disordered EHO-OPPE clusters that are phase-separated from the UHMW-PE matrix. Most strikingly, Fig. 4.4 (c) exhibits well separated diffraction-limited fluorescent spots of variable intensity, organized in rows along the direction of tensile deformation. Many of these spots can be attributed to single EHO-OPPE molecules because of their characteristic blinking and stepwise photobleaching apparent from fluorescence time traces in Fig. 4.5. In Fig. 4.4 (c) and (d), the fluorescence signal recorded simultaneously for both polarization components at the corresponding positions is shown. The large difference in average fluorescence intensity between the polarization directions in Fig. 4.4 (c) and (d) clearly demonstrates on a molecular level the high degree of orientation of the conjugated molecules in the spots. This is in sharp contrast to the corresponding confocal images of the undeformed film (Fig. 4.4 (a) and (b)), where equal intensities are observed for both polarizations. Reference samples without EHO-OPPE show only very weak fluorescence, well below the count rate of typical single conjugated polymer fluorescence spots. The number of fluorescent spots observed in the oriented blends was found to scale linearly with the nominal concentration of conjugated polymer, but typically ac-



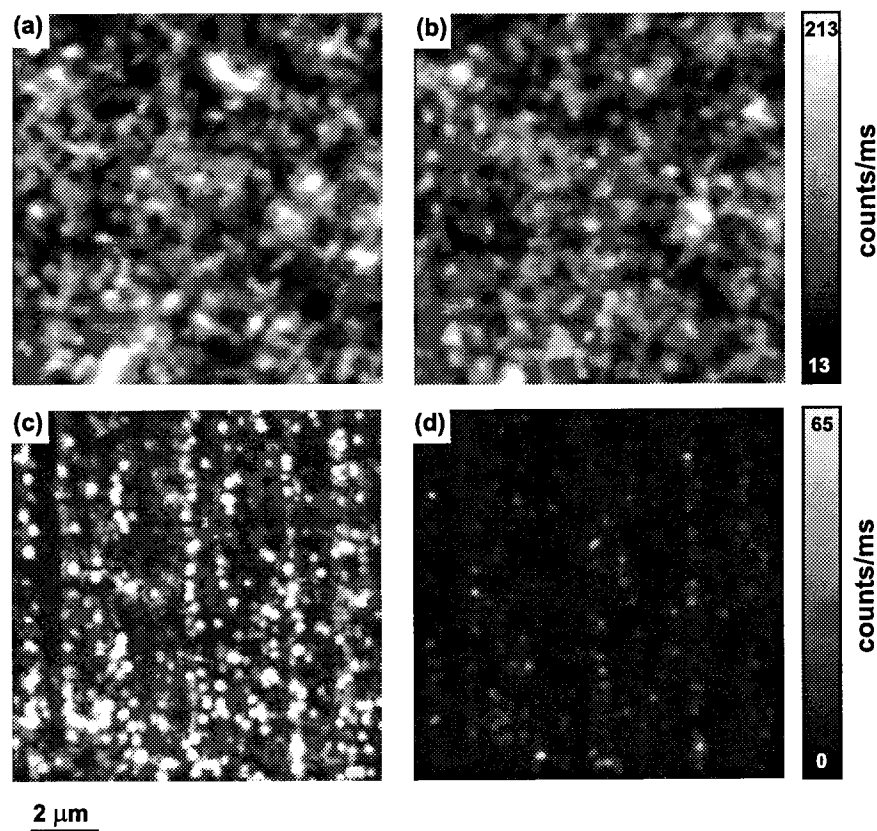


Figure 4.4: SCOM images of dilute ( $10^{-4}\%$  w/w EHO-OPPE) films prior to ((a) and (b)) and after stretching ((c) and (d)). (a) and (c) show the polarization component along the axis of stretching, (b) and (d) the orthogonal component. While no preferential orientation or morphology can be detected before deformation, the fluorescence intensity appears primarily as separated spots in the polarization channel along the direction of tensile deformation in (c).

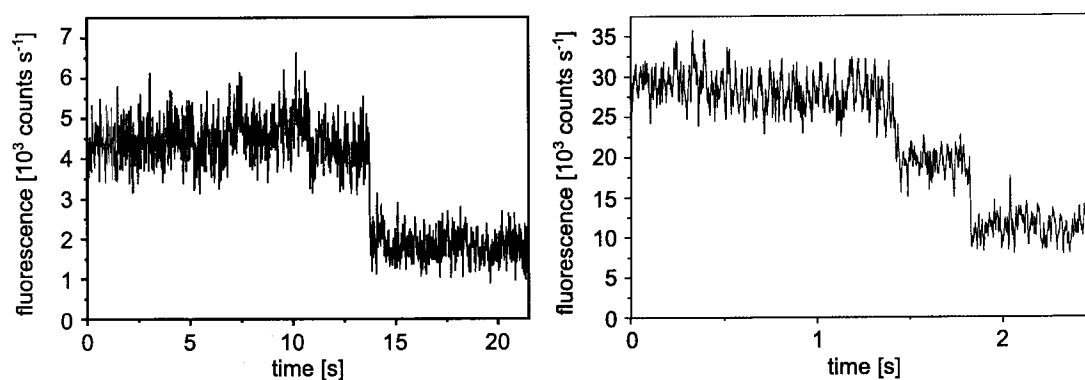


Figure 4.5: Fluorescence time-traces acquired on individual fluorescent features. The left time-trace shows a single step-like bleaching event. The right trace shows two steps of equal height, indicating the presence of two photophysically identical molecules.

counts for only about 12% of the nominal EHO-OPPE concentration. This finding is in agreement with previous single-molecule studies of conjugated polymers [49,50] and is consistent with the existence of non-luminescent molecules, an uncertainty in molecular weight of EHO-OPPE, and actual losses of the latter during sample preparation. Additional time-traces acquired on fluorescence spots in the deformed films often show bleaching in several steps of equal intensity (Fig. 4.5), suggesting that the brighter spots observed in Fig. 4.4 (c) and (d) represent clusters of multiple chromophores. Interestingly, the degree of deformation-induced orientation appears to be a function of cluster size. Weaker spots, in general, were found to be predominantly visible in the parallel polarization image (compare Fig. 4.4 (c) and (d)), consistent with a high degree of orientation of the respective chromophores. More intense spots, on the contrary, show the tendency to be also visible in the perpendicular polarization direction, indicating a reduced orientation of the EHO-OPPE molecules when clustered. In view of the short, rigid, rod-like conformation of EHO-OPPE, and the long, flexible shape of UHMW-PE, this fact seems plausible: Isolated EHO-OPPE molecules interact only with UHMW-PE molecules, and are thus strongly forced to take on the preferential matrix orientation, whereas clustered EHO-OPPE molecules rather experience interactions among themselves. In view of their less elongated shape, it is therefore more likely, that they are in a disordered state.

## 4.5 Quantitative Analysis

In order to obtain more quantitative information on the degree of clustering and orientation of single EHO-OPPE molecules as a function of deformation ratio, large areas ( $\sim 25 \times 25 \mu\text{m}^2$ ) of stretched films ( $10^{-4}\%$  w/w EHO-OPPE) were imaged by scanning confocal optical microscopy. A non-linear least-square fit of fluorescence spots in the images to two-dimensional Gaussians was performed using the Levenberg-Marquard algorithm [51] which determines their center, integrated intensity, the local background, and the respective errors. All subsequent statistical evaluations are based on fluorescent spots with a peak height exceeding the local background by a factor of at least three, and which met the additional requirement

that the error [51] of the intensity parameter did not exceed 20% of the integrated intensity. By applying these two empirical criteria, fits of poor quality in areas with large background signal, or due to photobleaching are discarded without introducing a bias for any particular cluster size. Each fluorescence spot, which corresponds to a single molecule or a small cluster of molecules, is fitted, providing an estimate of the statistical distribution of intensities, i.e. a pdf, as outlined in chapter 3.2.1. Combining all individual pdfs for accepted fluorescence spots (typically about 100 for a given  $\eta$ ) results in pdfs that characterize the probability distribution for measuring a certain integrated intensity on a randomly selected fluorescent spot. Fig. 4.6 shows

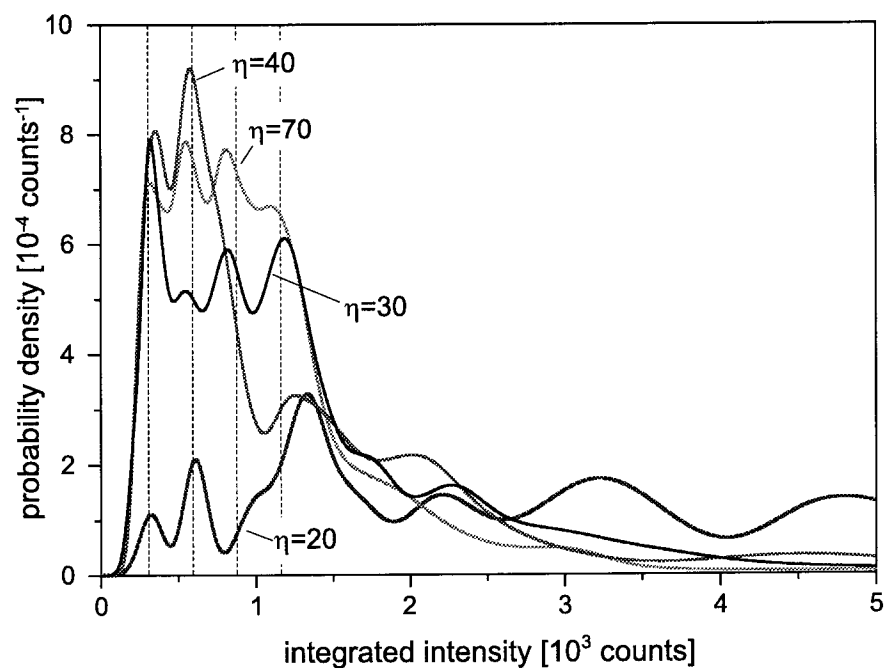


Figure 4.6: Intensity probability density functions for EHO-OPPE/UHMW-PE films of varying draw ratios  $\eta$ . The predominance of small cluster sizes for large values of  $\eta$  is clearly seen.

such combined pdfs for films of various draw ratios. At smaller integrated intensities, the combined pdfs show, independent of  $\eta$ , well-defined equidistant maxima (inset in Fig. 4.7), evidencing the presence of an integer number of chromophores in each cluster. The total probability for measuring a given cluster size (i.e. the number of chromophores comprised in a cluster) can be deduced from such combined pdfs by fitting with a sum of Gaussians yielding peak positions and relative weight of the first 4 peaks [24]. Clusters with a size  $> 4$  cannot be unambiguously

assigned to an integer multiple of the basic intensity while, however, still contributing to the pdf with the appropriate statistical weight. This behavior is related to an increasing error in the intensity measurement, due to increased photobleaching probability, and an intrinsic broadening of individual pdfs due to noise [24]. The obvious increase in the occurrence of single chromophores and bi-chromophoric clusters with increasing deformation ratio (Fig. 4.6) at the expense of the number of larger clusters shows the increased degree of molecular dispersion of initially phase-separated domains. This effect is illustrated by comparing, for example, the combined pdfs for  $\eta = 30$  and  $\eta = 40$ . The probability to find single chromophores and bi-chromophoric clusters is strongly increased for the latter. For the  $\eta = 70$  pdf, a strong decrease in the statistical weight of larger clusters is observed, while the weight of the first three peaks is approximately equal. The statistical weight

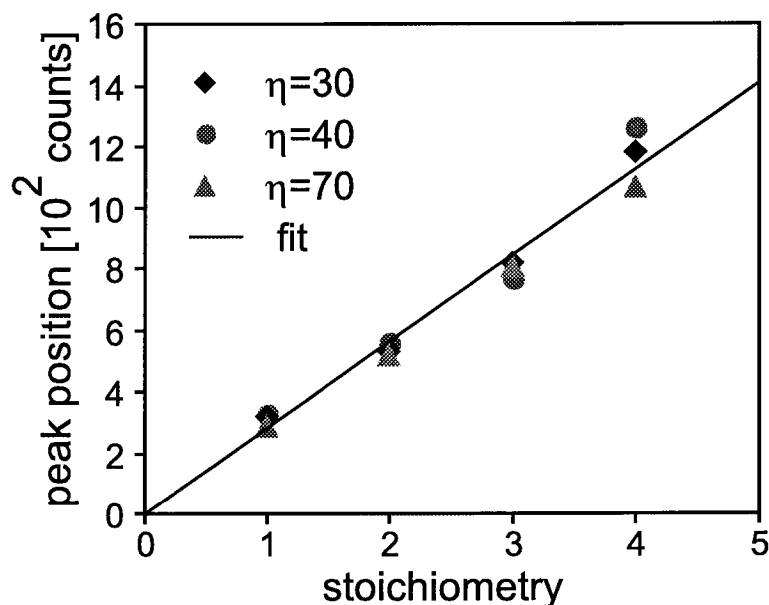


Figure 4.7: Average integrated cluster intensity vs. assigned stoichiometry for different  $\eta$ . The strictly linear dependence, which extrapolates to zero, shows that a single, well defined chromophore is observed.

of single chromophores and bichromophoric clusters in the latter sample is actually slightly smaller than for  $\eta = 40$ . This finding probably originates from minor local inhomogeneities in the films that could not completely be averaged out, although at least two images recorded at different locations were evaluated. Still, the combination of additional wide-field fluorescence and scanning confocal optical images

suggests that the presently employed (unstretched as well as stretched) dilute blend films are, on a large scale, rather homogeneous with respect to size and distribution of EHO-OPPE clusters. Thus, the results obtained from scanning confocal optical images seem to adequately reflect the "average structure" of the films and Fig. 4.6 provides clear quantitative evidence for a deformation-induced molecular dispersion of small clusters, ultimately leading to blends that comprise a significant fraction of isolated single chromophores.

The number of fluorescent units, as determined according to 3.2.1, is not necessarily equivalent with the number of EHO-OPPE molecules, for several reasons: Some of the EHO-OPPE molecules can be nonluminescent due to formation of trapping sites on the polymer backbone, which permit radiationless relaxation. Further, the absorption spectrum of EHO-OPPE is not consistent with its physical size, but rather indicates an effective conjugation length, which is much smaller. For this reason, it cannot be excluded, that several chromophore units can be found on a single EHO-OPPE molecule. However, the fact that the peaks in Fig. 4.6 are found at well-defined, equidistant positions, indicates the presence of a well-defined chromophore.

## 4.6 Deformation-induced Orientation

To address the issue of deformation-induced orientation of the molecules, the average dichroic ratio of isolated fluorescence spots was determined as a function of  $\eta$  by dividing the integrated intensities of fluorescence spots occurring at the same position in the two orthogonally polarized fluorescence images. The results, which are obtained for the same set of fluorescence spots as used for Fig. 4.6, are plotted in Fig. 4.8. It is seen that an almost complete orientation of the molecules occurs for the draw ratio range  $\lambda = 20..40$ . Gratifyingly, the dichroic ratio increases with increasing draw ratio and reaches saturation around  $\eta = 40$ , in perfect accord with results obtained in previous macroscopic studies [40], and also the dispersion-behavior reflected by Fig. 4.6.

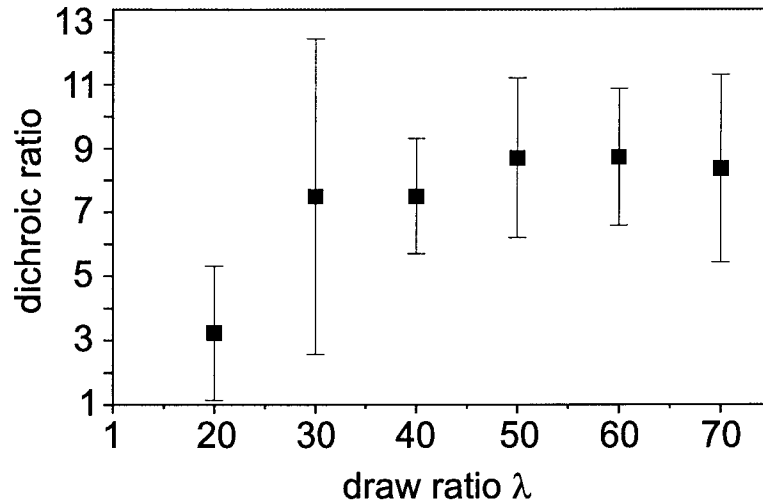


Figure 4.8: Average dichroic ratio as a function of  $\eta$ . In accord with ensemble studies, saturation sets in at  $\eta \approx 40$ . The low maximum value is due to background fluorescence.

## 4.7 Conclusions

Molecular rearrangements taking place during the solid-state tensile deformation of an initially phase-separated polymer blend have been demonstrated. Deformation-induced molecular dispersion of highly incompatible polymers was demonstrated at the example of EHO-OPPE in polyethylene. Dispersion of the molecules within the matrix and orientation occur concomitantly, indicating that interactions between the short, rigid-rod-like EHO-OPPE molecules and the UHMW-PE matrix give rise to orientation of EHO-OPPE. Consistently, clusters of EHO-OPPE molecules are characterized by local orientational disorder.

# 5. Statistical Analysis of Single-Molecule Colocalization Assays

In this chapter, it is shown that dual-colour single-molecule microscopy can serve as a highly efficient method for screening of molecular recognition events. Both ligand and receptor molecules of interest carry differently coloured dye molecules as labels. This enables highly accurate determination of their intermolecular distances. A statistical formalism for assigning binding probabilities is introduced. It is shown that on the basis of this formalism, few binding events suffice to decide beyond any doubt, whether two molecular species exhibit specific molecular recognition, or not.

## 5.1 Introduction

A frequent problem in analytical assays is that usually small quantities of analyte are to be detected with highest reliability in the presence of a multitude of other, often unknown substances. Therefore, e.g., fluorescence, absorption or radioactivity due to specific binding between a ligand and a receptor has to be discriminated from a respective unspecific background. In order to account for this background, conventional techniques rely on reference measurements to quantify the amount of unspecific signal [52]. For assays with ever smaller quantities of reagents this strategy ceases to be meaningful, when the uncertainty in background determination exceeds the signal due to specific recognition, thus setting a lower limit for the precise quantification of amounts of substance. This inherent problem can be overcome, e.g. by applying an assay architecture where specific binding is detected, by monitoring signals exclusively due to the close proximity of ligand and receptor [53–56]. A key advantage of single-molecule techniques is their ability to circumvent averaging. Hence it becomes possible to unravel correlations of individual events rather than detecting changes of average values [15, 57]. With respect to analytical applications this means that probabilities for the occurrence of an event of interest can be quantified on a single-event basis [20]. The introduction of quantitative single-molecule assays to applied analytical chemistry thus should result in important improvements, since the detection of minute quantities of substances accompanied by a strong background becomes feasible, making realistic applications in forensics or environmental protection conceivable [58–61]. The increased experimental efforts associated with single-molecule techniques can be justified for two reasons: (i) Diagnosing a disease at an early stage, where examination of only a small amount of tissue taken from a patient needs to yield unambiguous results [61]. To a similar extent, (ii) developments towards increased throughput of screening methods or the miniaturization of assays call for the detection of minute quantities of analyte leading to digital chemical analysis in the ultimate limit. Here, a general statistical approach for the evaluation of colocalization assays by dual-colour single-molecule imaging is introduced. Based on the very high spatial accuracy achieved in single-molecule imaging [23, 60, 62–65], distances between individual immobilized ligand-receptor pairs [60, 62] can be determined well below the resolution limit. The ensemble of



pairs is composed of two distinct subsets: in addition to those pairs that are actually bound, ligands and receptors can also be found in close proximity at random due to unspecific adsorption to the surface. Starting from well-known expressions for the distributions of distances in either case, a measure for the probability of correct assignment of a single receptor-ligand pair as a function of its detected intermolecular distance is constructed. To demonstrate the power of the present approach, the method is applied to the analysis of a single-molecule DNA hybridization assay described previously [60]. In contrast to previous findings, where a diagnosis was made on the basis of 289 observations, a few observations now suffice to confidently establish a diagnosis based on a predefined quantitative criterion.

## 5.2 Experimental

The substrate consisted of a phospholipid bilayer deposited onto a clean microscopy cover slip. Immobilization of single-stranded DNA target sequences to the substrates was performed via biotin-streptavidin linkage, where the streptavidin molecules were labeled for green-excitation. Complementary single-stranded DNA probe sequences were labeled for red-excitation. After the substrate preparation procedure, the red-labeled probe sequences were allowed to bind to the green-labeled target sequences during a 10 minute incubation period, followed by thorough washing steps to expel unbound probes from the surface. For a more detailed description of the preparation procedures, see [60].

## 5.3 Microscopy

A wide-field microscopy setup was used for acquisition of microscopy images showing the spatial distribution of red- and green-labeled molecules, respectively. In contrast to the setup discussed in 3.1.1, two acousto-optic modulators allowed for switching between the 514 nm line of an Argon ion laser and the light of a dye laser tuned to 632 nm, for selective excitation of green and red molecules. In [62], the microscopy setup is described in detail. Careful calibration of the apparatus excluded systematic

sources of error, such as vibrations and chromatic aberrations, demonstrating that red and green microscopy images are in accurate spatial registry. As discussed in chapter 3.1.2, the fluorescence pattern observed for a single molecule can be fitted to a two-dimensional Gaussian, precisely revealing the lateral position of the molecule. A series of test measurements with dual-color labeled single molecules [62], followed by a fitting procedure proved an accuracy of 38 nm for measuring the distance between red and green molecules. Fig. 5.1 shows single-molecule fluorescence images obtained in the hybridization assay. Two images taken at the same sample spot in sequence show the distribution of red- and green-labeled molecules, respectively. After running a binding assay with fluorescence-labeled molecules, a concentration

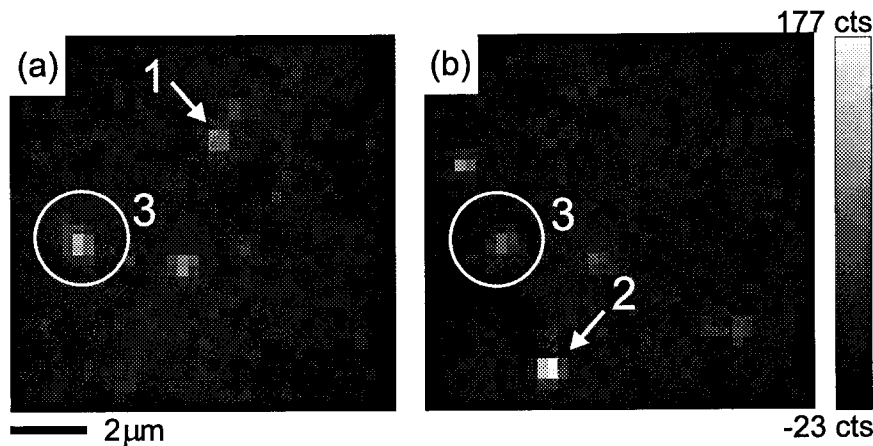


Figure 5.1: Dual-colour imaging of receptors and ligands. (a) shows the distribution of green-labeled receptor molecules, (b) the distribution of red-labeled ligands. The molecules (3), which are circled in (a) and (b), are at coincident spatial positions, indicating a hybridization event, whereas (1) and (2) are isolated receptor and ligand molecules, respectively.

$c_R$  of molecules of species R (ligand molecules; here: DNA probe sequences) and a concentration  $c_G$  of molecules of species G (receptor molecules; here: DNA target sequences), respectively, are found immobilized on a surface. R indicates labeling for red-, G for green-excitation, respectively. Three different types of events may be distinguished (see Fig. 5.1) : a) Isolated green receptor molecules (1), b) isolated red ligand molecules that are unspecifically adsorbed to the surface (2), and c) specific binding events, characterized by red and green spots, i.e. ligand and receptor molecules in close proximity, as indicated by the circles (3) in Fig. 5.1.

## 5.4 Theory

There are two distinct cases for the observation of a ligand R: (i) a ligand molecule R which is specifically bound to an receptor G (probability  $p(s)$ ,  $s$  for specific binding), and (ii), a molecule R unspecifically adsorbed to the surface ( $p(u) = 1 - p(s)$ ,  $u$  for unspecific binding). The probabilities  $p(s)$  and  $p(u)$  can be determined straightforwardly from an ensemble measurement of specific or unspecific binding. In practice, this is done by performing binding experiments with two substrates, one with receptors, one without receptors. On average, there are  $p(s)c_R$  R-G pairs per surface unit due to molecular recognition events, where  $c_R$  is the surface density of R molecules. All the remaining  $p(u)c_R$  R molecules that do not belong to the abovementioned pairs, are unspecifically adsorbed on the surface (if, as in our case, there are less receptors (G) than ligands (R)). The goal of the present analysis is to calculate molecular recognition probabilities for all pairs on a one-by-one basis. In order to arrive at a quantitative description, the following strategy is pursued: From first principles, conditional probabilities for observing certain intermolecular R-G distances given the assumption that the molecules are specifically (unspecifically) bound to the substrate are derived. Exploiting the knowledge of  $p(s)$  and  $p(u)$ , probabilities for specific (unspecific) binding given a certain measured intermolecular distance for an individual pair of R and G molecules can be assigned. To provide a basis for the analysis of the data, a simple computer algorithm generates an ideal assignment of R-G pairs found in images. The algorithm is devised such that it finds the most likely out of all possible pair-assignments, i.e. the one for which the sum of all intrapair R-G distances is minimal. This provides a list of distances between the assigned R-G pairs. At first, the probability density function (pdf) for intermolecular distances of an R-G pair in Cartesian coordinates is derived:

$$\rho(\delta x, \delta y) d\delta x d\delta y \propto \exp\left[-\frac{(\delta x - \Delta x)^2 + (\delta y - \Delta y)^2}{4\sigma^2}\right] d\delta x d\delta y \quad (5.1)$$

which is simply a two-dimensional Gaussian distribution reflecting the measurement uncertainties centered around the actual distance  $\Delta x$  in x-direction and  $\Delta y$  in y-direction, respectively. Here,  $\sigma$  is the standard deviation of the microscope for locating the position of a molecule, which can be determined independently [23]. Eq.

5.1 can be transformed to polar coordinates using  $\delta x = r \cos\varphi$ ,  $\delta y = r \sin\varphi$ ,  $\Delta x = r' \cos\vartheta$  and  $\Delta y = r' \sin\vartheta$ , where  $r$  is the actual physical distance between two molecules and  $r'$  is the measured distance. For symmetry reasons,  $\varphi$  is set to zero, and integration over  $\vartheta$  performed using the surface element  $dA = r' dr' d\vartheta$ , yielding:

$$\rho(r' | r) dr' = \frac{1}{2\sigma^2} r' \exp\left[-\frac{r^2 + r'^2}{4\sigma^2}\right] I_0\left[\frac{rr'}{2\sigma^2}\right] dr' \quad (5.2)$$

where  $I_0$  is the zero-order modified Bessel function of the first kind. The function  $\rho(r | r') dr'$  (eq. 5.2) describes the probability to measure a distance  $r'$  between an R-G pair given that the actual distance is  $r$ . This pdf fully characterizes the distribution of intermolecular distances that would be obtained from repeated distance measurements on one and the same pair of molecules. For the special case of specific binding (case s) between two molecules, the pdf of the measured distance  $r'$  is obtained from eq. 5.2 by setting  $r = 0$ , yielding

$$\rho(r' | s) dr' = \frac{1}{2\sigma^2} r' \exp\left[-\frac{r'^2}{4\sigma^2}\right] dr' \quad (5.3)$$

Assuming a random distribution of molecules, one can also derive an expression for the pdf for incidental proximity (case u) of an unspecifically adsorbed molecule R to a molecule G [66]:

$$\rho(r | u) dr = 2\pi r p(u) c_R \exp(-r^2 \pi p(u) c_R) dr \quad (5.4)$$

$\rho(r | u)$  is the probability density for an intermolecular distance  $r$ , given the pair of molecules is not colocalized. In order to account for the measurement uncertainty in determining intermolecular distances, this pdf has to be convolved with the expression for  $\rho(r' | r)$  (eq. 5.2), yielding

$$\rho(r' | u) = \int \rho(r' | r) \rho(r | u) dr = \frac{2\sigma^2}{1 + 4\pi p(u) c_R \sigma^2} \exp\left[-\frac{r'^2 \pi p(u) c_R}{1 + 4\pi p(u) c_R \sigma^2}\right] \quad (5.5)$$

The quantities of interest are  $p(s | r')$  and  $p(u | r') = 1 - p(s | r')$ , the probabilities for specific binding or incidental vicinity given the measured distance  $r'$ . Above,  $\rho(r' | s)$  and  $\rho(r' | u)$  have been derived, which are related to the desired function

$p(s | r')$  by Bayes' theorem [22]:

$$p(s | r') = \frac{p(s)\rho(r' | s)}{p(s)\rho(r' | s) + p(u)\rho(r' | u)} \quad (5.6)$$

The function  $p(s | r')$  is found by substituting 5.3 and 5.5 into 5.6. Thus, it is possible to generate a "look-up table" that can be consulted to assign a probability for specific binding to each measured distance. The possibility to refer to a look-up table is instrumental for the kind of fast analysis ultimately needed in a screening assay [67]. Fig. 5.2 shows the typical behavior of the lookup-table  $p(s | r')$  for the set of parameters given in the figure caption. The function  $p(s | r')$ , corresponding to the DNA wide-field experiment, is plotted as a solid line. As is evident, for distances larger than 200 nm the probability for specific binding is negligible. The dashed line holds if, e.g., near-field optical microscopy was used to image the molecules. It is evident that the increase in spatial resolution results in a significantly improved statistical confidence for discriminating specific binding events. Interestingly, both lookup tables decay towards zero for  $r' \rightarrow 0$ , which is a consequence of the fact that due to measurement uncertainties, it is extremely unlikely to observe a distance of zero between colocalized molecules.

## 5.5 Results and Discussion

Fig. 5.3 shows a probability series obtained for all 289 pairs of molecules found in the DNA hybridization experiment. Grouping of all green and red molecules into pairs was performed with a least-distance algorithm, yielding the most likely assignment. The probabilities were obtained from the set of measured R-G distances using the look-up table 5.6 plotted in Fig. 5.2. Most strikingly, it is observed that the 289 pairs are clearly divided into two distinct categories: (i) those that exhibit values of  $p(s | r')$  close to zero (94%) and (ii) those that have high  $p(s | r')$  values, indicating high probabilities for specific binding (6%). This finding is a clear result of the sigmoidal shape of the look-up table in Fig. 5.2. The use of a higher resolution microscopy would lead to even more distinct results. It should be pointed out that the continuous function used as look-up table permits an objective quantification of

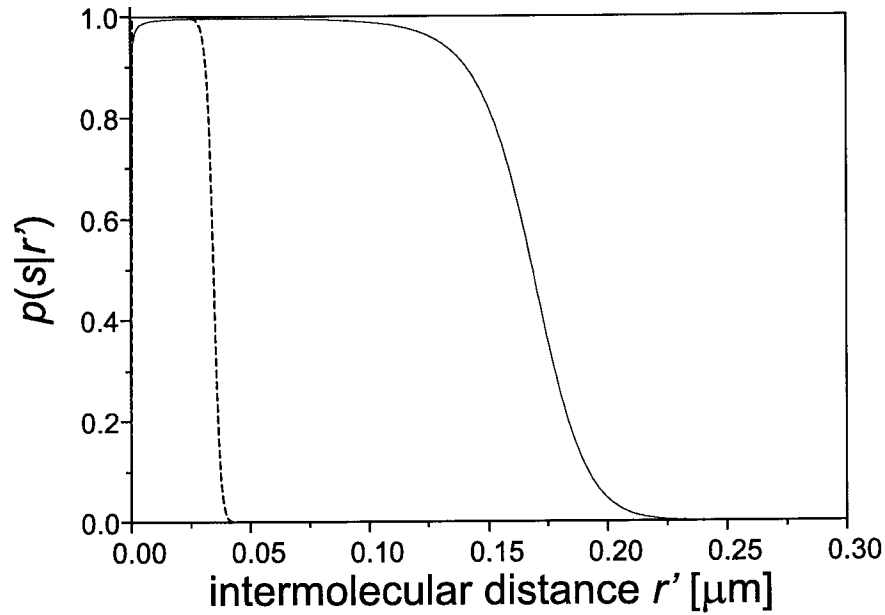


Figure 5.2: Lookup-table generated from eq. 5.6. The solid curve holds for the experimental parameters in this study ( $p(s) = 0.05$ ,  $\sigma = 30 \text{ nm}$ ,  $c_R = 0.1 \mu\text{m}^{-2}$ ), the dashed curve would be obtained for typical near-field parameters ( $p(s) = 0.05$ ,  $\sigma = 5 \text{ nm}$ ,  $c_R = 0.1 \mu\text{m}^{-2}$ ).

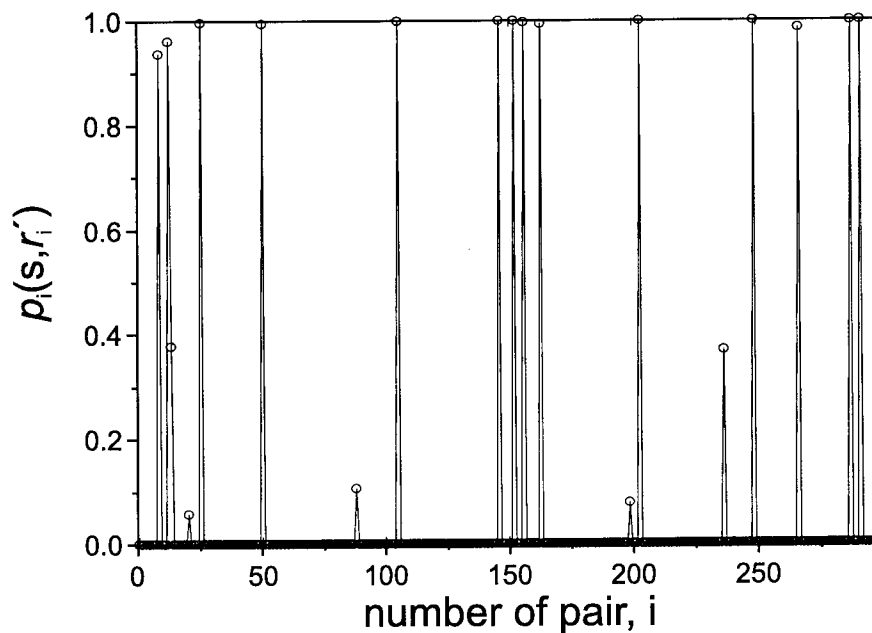


Figure 5.3: Series of single-event probabilities, obtained by application of the lookup table (5.2). Due to the sigmoidal shape of the lookup-table, the events are clearly categorized into likely and unlikely ones.

the probability for specific binding for any measured intermolecular distance. In an earlier analysis [60], the simplified assumption was made that specific binding had occurred in cases where intermolecular distances smaller than  $\sigma$  were measured. In view of the present analysis this corresponds to approximating the look-up table derived here by a radial step function. The drawback of this simple approach is that the assignment of results is purely binary and that there is no quantitative value for the likelihood of an error. Therefore, the previous work had to rely on all 289 events in order to arrive at a conclusion about the single-molecule colocalization assay [60]. In contrast, the present methodology, while being consistent with the step-function approach, permits the full statistical description of a single observation, i.e. the probability for the truth of a given hypothesis (i.e. "specific recognition has occurred") can be quantified accurately.

Up to this point, it has been shown that single pairing events can be characterized quantitatively. However, when analyzing the outcome of a single-molecule colocalization assay in general one has to deal with multiple events, i.e. a small set of pairing events. It is a challenge with respect to diagnostic applications to come up with a statistically sound method that enables to make decisions on the basis of a small set of observations. For a reliable judgement, it should be possible to calculate the probability that no recognition took place, which e.g. in medical applications would correspond to a negative diagnosis. From a naïve point of view, this is easy to accomplish: Multiplying the values of  $p_i(u | r')$  of all observed pairs yields the probability

$$p_0 = \prod_i p_i(u | r') \quad (5.7)$$

that all individual pairing events were unspecific corresponding to the probability for a negative outcome of the assay. Although this simple consideration is correct, it may be misleading. This can be demonstrated at the example of a worst-case scenario consisting of a hypothetical experiment in which every individual pairing event is characterized by  $p_i(u | r') = p_i(s | r') = 0.5$ . Because there is equal probability for both, recognition and unspecific binding, this experiment evidently does not provide any information! Judging from eq. 5.7, however, one would conclude based on only 7 observations that the probability for a negative outcome of the assay is less than 1%. From this consideration it is obvious that additional information

is required in order to establish a *reliable* diagnosis. Therefore, a more complete characterization of the experiment has to be found. A diagnosis based on the assay should rely on two characteristic figures: (i) the probability that the outcome of the assay is negative which is provided by  $p_0$ , eq. 5.7, and (ii) the quality of the measurement in comparison to other measurements (and hence: how reliable is the value determined in (i)). To establish both, a measure of reliability and the desired value for the probability that the outcome of the assay was negative, the following strategy is proposed: Having observed  $N$  individual pairs in an experiment, a set of probabilities  $\{p_1(s | r'_1), p_2(s | r'_2), \dots, p_N(s | r'_N)\}$  is obtained. The experiment is completely characterized by specifying the probabilities for all possible outcomes, i.e. the  $N$  probabilities  $p_m$  for the truth of the statements: " $m \leq N$  events out of  $N$  pairs observed in total were due to specific recognition". These probabilities are obtained by applying similar considerations that lead to the binomial distribution. However, in contrast to a binomial distribution, which would be determined by only two constant probabilities  $p(u | r')$  and  $p(s | r')$  applying to each of the  $N$  individual events, the more general case, where each event is characterized by different probabilities  $p_i(u | r')$  and  $p_i(s | r')$ , has to be considered. The probability values assigned to each individual pair of molecules (eq. 5.6) are thus combined to generate the discrete probabilities  $p_m$ . In order to obtain the  $p_m$ , a combinatorial algorithm is applied that generates all possible outcomes of the experiment with their respective probabilities. If  $S_m$  denotes the set of possibilities  $S_{kn}$ ,  $n \in \{1, \dots, \binom{N}{m}\}$ , of choosing  $m$  values out of the set  $\{p_1(s | r'_1), p_2(s | r'_2), \dots, p_N(s | r'_N)\}$ , and  $\bar{S}_{kn}$  is its complementary set, then

$$p_m = \sum_k \prod_{i \in S_{kn}} p_i(s | r'_i) \prod_{i \in \bar{S}_{kn}} (1 - p_i(s | r'_i)) \quad (5.8)$$

i.e. the sum over all possible joint probabilities resulting in  $m$  specific recognition events and  $N-m$  incidental events. In other words, if  $p_m$ , the probability for  $m$  specific events, is desired, all possibilities of picking  $m$  pairs out of the entire set of  $N$  have to be considered. For example, in the case  $N = 4$ , where  $n \in \{1, \dots, 4\}$ ,  $S_3$  reads  $S_3 = \{S_{31}, S_{32}, S_{33}, S_{34}\} = \{\{p_1, p_2, p_3\}, \{p_1, p_2, p_4\}, \{p_1, p_3, p_4\}, \{p_2, p_3, p_4\}\}$  and  $\bar{S}_3 = \{p_4, p_3, p_2, p_1\}$ . For each of the subsets  $S_{kn}$ , one can calculate the joint probability that the events in  $S_{kn}$  were indeed specific binding events,



whereas all other  $N - m$  events in  $\bar{S}_{kn}$  were unspecific by forming the product of the respective  $p_{i,s}$  and  $p_{i,u} = 1 - p_{i,s}$ . By summing all of the latter, over the index  $k$ , as is done in eq. 5.8, one arrives at the probability  $p_m$  that any  $m$  pairs out of  $N$  were specific binding events. This distribution represents the most complete characterization of the hybridization experiment that is possible on the basis of the measured data. The distribution of probabilities  $p_m$  contains the desired diagnosis parameters straightforwardly: (i) the probability that the outcome of the assay is negative is given by  $p_0$ . The quality of the measurement, (ii), is obviously characterized by the width of the distribution of  $p_m$  values. A very narrow, sharply peaked distribution will clearly indicate one distinct outcome of the experiment as most likely, whereas broad distributions yield less information. With this idea in mind, a measure of quality  $q$  is defined that ranges from  $q = 0$  for experiments void of information to  $q = 1$  for ideal experiments, i.e. conditions, under which the outcome of the experiment can be assigned unambiguously. Considering again the worst-case experiment discussed above that did not yield any information, a binomial distribution for the probability 0.5 would be obtained for the  $p_m$  values. This worst-case distribution has a standard deviation of  $\frac{1}{2}\sqrt{N}$ . Consequently,

$$q = 1 - \frac{2\sigma(p_m)}{\sqrt{N}} \quad (5.9)$$

fulfills the defined requirements. Here  $\sigma(p_m) = \sqrt{\sum_i p_i(i - \bar{m})^2}$  is the standard deviation of the distribution of  $p_m$  values, where  $\bar{m} = \sum_i ip_i$ . The function  $q$  can be used to determine, which of various possible experimental assays is best suited for obtaining a diagnosis. Taking into account these two criteria, the relevant conclusions from a given experiment can be drawn: A diagnosis can be obtained with a quantitative, predefined criterion (e.g.  $p_0$  must be smaller than 1 %); the quality of this diagnosis can be quantified by its  $q$ -value and thus be compared to other experiments. In the worst-case scenario discussed above, one would obtain  $q = 0$ , although  $p_0$  is very small, and consequently, no diagnosis could be given.

To demonstrate this methodology, the total set of 289 measured pairs was randomly split into subsets of 20 pairs. Each of the subsets can be considered as an experiment where it is necessary to give a reliable diagnosis based on only few events. For each of

the subsets, the probabilities  $p_m$  were calculated as defined in eq. 5.8. On the left side of Fig. 5.4, the  $p_m$  values obtained for one exemplary subset of 20 pairs are plotted (filled circles). The maximum value of  $p_m$  is found for  $m=3$ . More importantly, it is seen that (i)  $p_0 \approx 0$ , indicating a positive outcome of the assay. Furthermore, (ii) the distribution exhibits a small width resulting in a value of  $q$  close to 1 ( $q \approx 0.75$ ), underscoring the reliability of the statement made in (i). The average number of successful binding events deduced from the  $p_m$  reflects the chemical affinity between ligand and receptor. In particular, the experimental  $p_m$  distribution is indicative of low binding affinity, as is evident from the fact that it is centered at  $m = 3$ . For other subsets,  $p_m$  distributions with maxima at different positions, but of similar shape are found. Also plotted in Fig. 5.4 is a binomial distribution for the parameter 0.5 as the limiting case for maximum uncertainty (filled diamonds), as well as a Monte-Carlo simulation for very efficient (80 %) reaction conditions (sharp distribution, peaked at  $m = 16$ , at the right end of the interval, stars). For the present assay it can be seen that in spite of the low binding probability, the narrowness of the  $p_m$  distribution indicates a high statistical reliability of the diagnosis based on a small number of events.

## 5.6 Conclusions

In contrast to conventional ensemble assays, where only the total quantity of molecular species present in the detection volume can be measured, the approach presented here additionally takes advantage of spatial information by using intermolecular distance measurements. It is therefore possible to assign probabilities for specific binding and incidental proximity of individual pairs, rendering this methodology significantly more insensitive to unspecific adsorption events. In addition to single-pair analysis, a statistical methodology that allows for compiling any number of observations into relevant decision criteria, is demonstrated. In addition to specifying the probability for the diagnosis that molecular recognition has occurred ( $1 - p_0$ ), another relevant quantity has been deduced, i.e. a quality parameter  $q$ , which constitutes an objective measure for how reliably an experimental method assigns a certain outcome of an experiment as the most likely one. This parameter not only allows

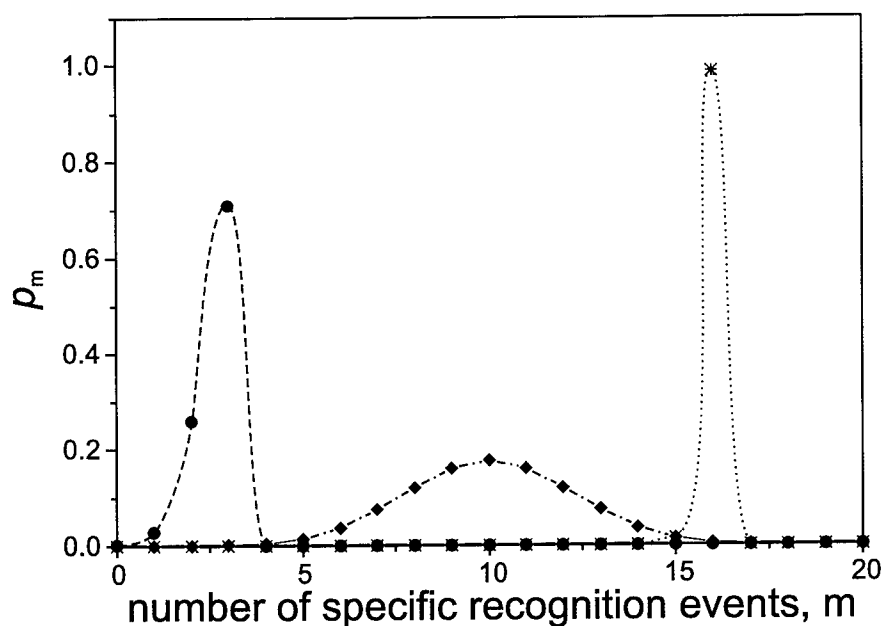


Figure 5.4: Discrete probability distributions for the possible experimental outcomes for sets of 20 observations. The left curve was obtained for the present experiment (5 % specific binding), the right curve is a Monte-Carlo simulation for efficient reaction conditions (80 % specific binding). The broad distribution in the center reflects a hypothetical experiment with minimum information content.

for judging the reliability of a diagnosis, but also provides an objective criterion for comparing different microscopy techniques for a certain analytic application. It is therefore possible to terminate an experiment after any number of observations, while a complete statistical characterization of the outcome is still possible. The measurements used to illustrate the potential of our analysis indicate that only few successful binding events are required to establish a reliable diagnosis. In particular, it has been shown at the example of an experimental model system, that 20 observations suffice for a highly reliable diagnosis. This finding is particularly intriguing in view of the fact that the resolution of the optical wide-field microscopy employed is poor in comparison to molecular length scales.



## 6. Continuous Real-Time Measurement of Fluorescence Lifetimes

In this chapter, a method for online measurement of fluorescence lifetimes is introduced. On the basis of the results of chapter 3.2.3, an average over excitation-emission time-lags of photons arriving within a sliding time window is calculated. Using a time-to-amplitude converter (TAC), the time-lags between excitation and emission for each photon are coded into a pulse sequence. Conversion of the pulse sequence into a continuous step function and subsequent low-pass filtering yield a signal proportional to the fluorescence lifetime of the molecule. A Monte-Carlo simulation demonstrates that this method outperforms a commonly employed scheme, especially at low count rates, while being easily implementable. The applicability of the proposed scheme is demonstrated by fluorescence lifetime imaging of individual molecules.

## 6.1 Introduction

Optical microscopy of fluorescent samples relies on the spatially resolved measurement of intensity and other spectroscopic parameters. Among these, the excited state lifetime of fluorescent molecules is often of particular interest, since it is both intensity-independent and sensitive to changes in the environment of the fluorophore [68]. Most commonly, fluorescence lifetimes are measured using so-called time-correlated single-photon counting (TCSPC), as described in chapter 3.2.3. However, the time-consuming process of fitting exponential decays prohibits the use of TCSPC in time-critical applications. A well-known approach to the real-time measurement of fluorescence lifetimes is based on modulating the excitation laser light and detecting the phase-shifted fluorescence. The magnitude of the phase-shift depends on the excited state lifetime [69]. As this method is based on lock-in techniques, it is restricted to strong fluorescence signals and analog detectors. In many fields of science and technology there is a strong need for handling ever smaller amounts of analyte and tendency for increasing the sensitivity to the single-molecule level. Therefore, in future photon-starved applications, where single-photon counting detectors are used, it is imperative to develop real-time techniques that can handle discrete sequences of photon counts for lifetime determination. Here, the so-called rapid-lifetime determination (RLD) method has been proposed in the past [70]. In RLD, the fluorescence counts are binned into two adjacent time windows following the laser pulse. The ratio of photon counts in the two time windows is used to calculate the fluorescence lifetime. While RLD is very accurate for large count rates, it encounters serious problems for lower count rates, since divisions by zero are encountered with increasing probability. Here, an alternative approach to realtime lifetime determination is presented, which is based on the fact that for a single-exponential decay, the fluorescence lifetime is equal to the average time-lag between an excitation laser pulse and the subsequent detection of a fluorescence photon. For each photon, a time-to-amplitude converter (TAC) generates a pulse of an amplitude proportional to the time lag between fluorescence photon and excitation pulse. The resulting sequence of pulses, with exponentially distributed amplitudes and interpulse times, is then subjected to a count rate independent averaging procedure.

## 6.2 Experimental

A TAC outputs a fixed-width pulse with an amplitude proportional to the time lag between a start and a stop pulse. As in TCSPC, the TAC is started by a photon pulse and stopped by the signal of a fast PIN-photodiode, which detects the arrival of the subsequent excitation laser pulse. The high repetition rate of pulsed lasers necessitates such reversed start-stop operation, which is common practice in lifetime measurements. Since the TAC is operated in reverse mode, longer excited state lifetimes on average result in *shorter* measured time intervals. As mentioned before, the lifetime of a single-exponential decay is equivalent to the average time lag between excitation pulse and fluorescence photon. Two count-rate independent ways of time-averaging the TAC output pulse sequence are suggested: (i) A fast analog to digital converter (ADC) can be used to digitize the pulse amplitudes and store them in a first-in-first-out (FIFO) memory for averaging. (ii) Averaging can also be achieved by conversion of the pulse sequence into a continuous step-function and subsequent low-pass filtering of the latter.

If low-pass filtering is to be applied, the conversion of the pulse sequence into a step function prior to averaging is mandatory: Time-averaging a function  $s_p(t)$ , which is a pulse-train, will yield proportionality both to the average count rate  $\langle f \rangle$  and the average pulse amplitude  $\langle a \rangle$ , since the integral over the function increases with the number of pulses per unit time:  $\frac{1}{T} \int_0^T s_p(t) dt \propto \langle f \rangle \langle a \rangle$ . For a step-function, this problem is eliminated, since the signal is continuously present, irrespective of the count rate. Generation of the continuous step-function  $s_c(t)$  is accomplished by sampling the voltage level of each TAC-pulse and maintaining it until the arrival of the next pulse. In Fig. 6.1, both an experimental pulse sequence (upper trace) and the corresponding step-function (lower trace) before filtering are shown. It should be noted that this type of signal treatment is not entirely equivalent to averaging the amplitudes of a number of pulses, as in approach (i). The stochastic interphoton times lead to varying step widths, giving rise to fluctuating statistical weights for each individual photon. In the following, it will be shown by analytic derivation that this peculiarity does not affect the outcome of the measurement on average, and is only a minor source of signal noise.

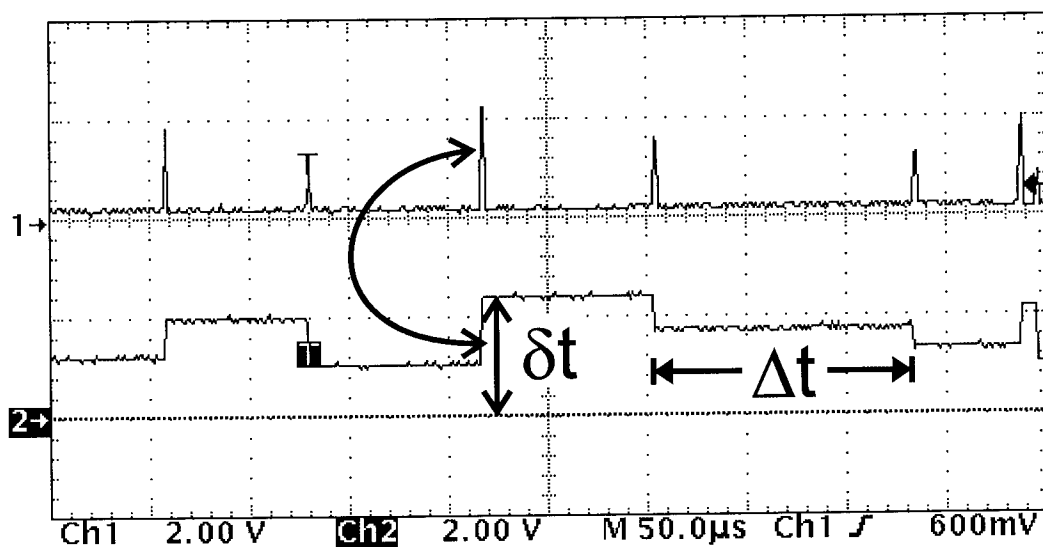


Figure 6.1: Illustration of the conversion process from the stochastic pulse sequence into a continuous signal at the example of experimentally measured data. At the arrival of each TAC-pulse, its voltage level is sampled and maintained until the next pulse, as is seen at the lower trace.

### 6.3 Theory

In the weak excitation regime, the time that elapses between the detection of two photons, i.e. the interphoton time, is exponentially distributed. Assuming that a photon was emitted at  $t = 0$ , the temporal probability density for the emission of the next photon at time  $\Delta t$  is given by:  $\rho_{\text{ipt}}(\Delta t) = f \exp(-f\Delta t)$ , where  $f$  is the average count rate and  $\Delta t$  is the interphoton time. The distribution of step widths  $\Delta t$  is thus given by  $\rho_{\text{ipt}}(\Delta t)$ . The second quantity that characterizes an individual step is its amplitude, which is proportional to the start-stop time lag. Its values are exponentially distributed as well:  $\rho_{\text{em}}(\delta t) = \frac{1}{\tau} \exp(-\frac{\delta t}{\tau})$ , where  $\tau$  is the fluorescence lifetime. Since  $\Delta t$  and  $\delta t$  are statistically independent, the two-dimensional probability density  $\rho(\Delta t, \delta t)$  for finding a step of length  $\Delta t$  and amplitude  $\delta t$  is given by:  $\rho(\Delta t, \delta t) = \rho_{\text{ipt}}(\Delta t) * \rho_{\text{em}}(\delta t) = \frac{f}{\tau} \exp(-f\Delta t) \exp(-\frac{\delta t}{\tau})$ . The time average of the step-function  $s(t)$ , corresponding to the low-pass filtered  $s(t)$  is given by:  $\langle s(t) \rangle = \frac{1}{T} \int_0^T s(t) dt$ , which can be written as a sum over  $n$  steps due to  $n$  photons emitted in the time interval  $T$ :  $\langle s(t) \rangle = \frac{1}{T} \sum_{i=1}^n \delta t_i \Delta t_i$ , where



the  $\delta t_i \Delta t_i$  are the areas of individual steps, and  $T = \frac{n}{f}$  is the time constant of the averager. Taking into account that the expectation value of the sum over  $n$  individual steps equals the  $n$ -fold expectation-value of one step, it is found that:

$$\langle s(t) \rangle = f \int_0^\infty \int_0^\infty \Delta t \delta t \rho(\Delta t, \delta t) d\delta t d\Delta t = \tau.$$

The figure of merit for an objective comparison of different lifetime determination schemes is the relative error  $\sigma_\tau/\tau$  of the lifetime signal as a function of the number  $n$  of photons in the averaging time window, where  $\sigma_\tau$  is the standard deviation of the lifetime signal. In order to evaluate  $\sigma_\tau/\tau$  for RLD, and the schemes (i) and (ii) proposed here, a Monte-Carlo routine for generating photon sequences obeying  $\rho(\Delta t, \delta t)$  was implemented. For each value of  $n$ , 400 sequences containing  $n$  photons

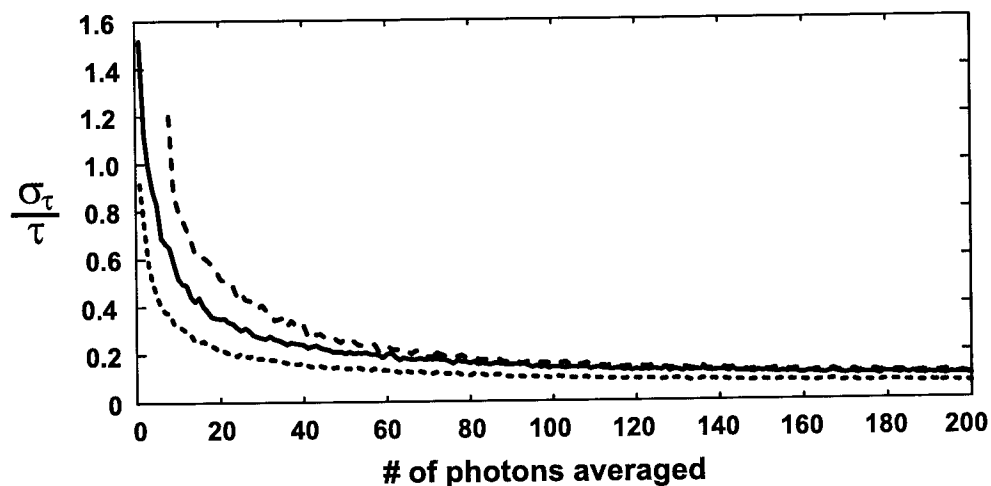


Figure 6.2: Monte-Carlo simulations of the experimental noise  $\sigma_\tau/\tau$  for the RLD method (dashed), the implemented scheme (i) (solid), and an optimal FIFO averager scheme (ii) (dash-dotted)

were generated and subjected to the algebraic operations that define RLD, methods (i), and (ii). At a given  $n$ , thus 400 estimates of the lifetime are obtained, from which both  $\tau$  and  $\sigma_\tau$  can be determined. Fig. 6.2 displays  $\sigma_\tau/\tau$  as a function of  $n$ . Large numbers of photons yield low noise for all three techniques. In the few-photon limit, RLD performs badly, since it involves frequent divisions by zero, which introduce additional noise. The averaging scheme (i) yields the best results, since it assigns equal statistical weights to each photon. Surprisingly, the scheme (ii) does

not introduce significantly higher noise, inspite of fluctuating statistical weights of the individual photons.

## 6.4 Results and Discussion

To experimentally demonstrate the feasibility of our concept, we implemented the relatively simple averaging scheme (ii). Fig. 6.3 depicts the electronic circuit used for pulse-amplitude averaging. The TAC pulses at the input of the circuit are

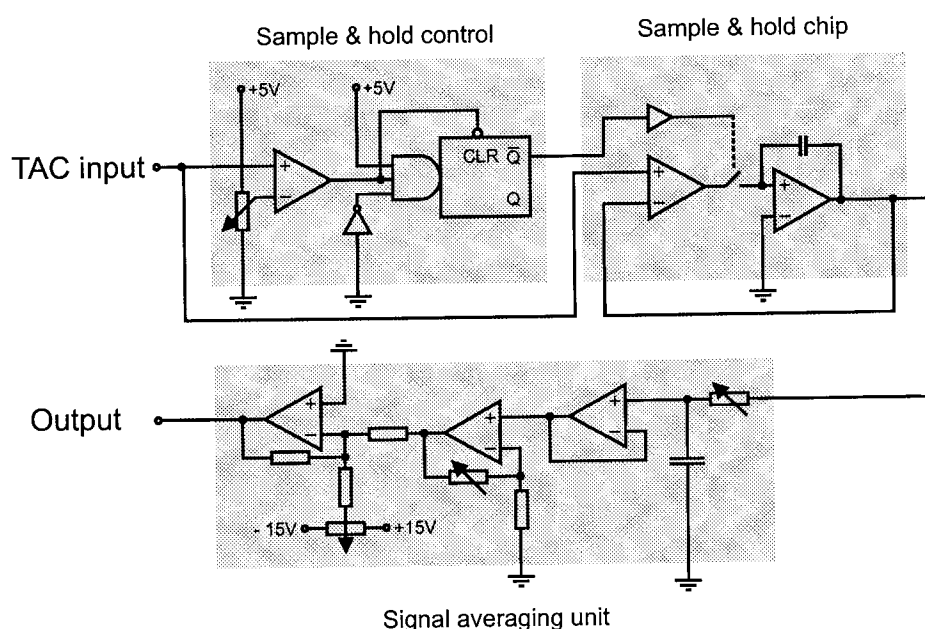


Figure 6.3: Sketch of the electronic circuit consisting of three units: The sample and hold control, which selects the time window for sampling of the TAC pulses, the sample and hold chip, which produces the step function, a variable cutoff frequency lowpass filter and a final stage for adjustment of offset and gain.

used to trigger a comparator with a selectable threshold voltage. When triggered, the comparator forces the monostable multivibrator to produce a single negative pulse of fixed length, which can be defined via an external RC-network (not shown in Fig. 6.3). The latter initiates the sampling period of a sample-and-hold chip. After the end of the sampling process, the sampled amplitude of the TAC input-pulse is maintained, until the arrival of the subsequent pulse. This results in a

step-function of the kind shown in Fig. 6.1. After averaging the signal by a low-pass filter with adjustable cut-off frequency, an inverting amplifier is used for signal amplification and correction of the reversed start-stop operation of the TAC. Finally, a further operational amplifier provides the possibility of adding offsets to the output voltage for calibration purposes. For an experimental demonstration, we interfaced our signal processing electronics to a scanning confocal optical microscope (SCOM). SCOM is frequently employed for single-molecule microscopy, where low count-rates are encountered. Since SCOM is a type of scanning microscopy, real-time image build-up is desired. The SCOM employed in this study is a conventional sample-scanning SCOM equipped with a single-photon counting avalanche photodiode (SPAD). An actively mode-locked Nd:YAG laser (Coherent Antares), frequency-doubled to 532 nm, is used as a light source that delivers 100 ps pulses with a repetition rate of 76 MHz. The TAC employed (Nuclear Enterprises, NE 4645) has a range of 5..50 ns. The gap in range has been accounted for by a delay line. The sample is prepared by dissolving *1,1'-dioctadecyl-3,3,3',3'-tetramethylindocarbocyanine* (DiI) with PMMA in Toluene and spincoating it onto cover slides. The cover slides were baked at 510°C to remove organic contaminants. Examination of the polymer film by atomic force microscopy revealed a smooth film with a uniform thickness of 30 nm. Fig. 6.4 shows simultaneously recorded fluorescence intensity (a) and lifetime (b) images. Some fluorescence spots in (a) are cut off due to discrete photobleaching. In (b), only those pixels of the image are displayed, for which the fluorescence intensity in (a) significantly exceeds the background count rate. This is commonly done in lifetime imaging, since the signal shows excessive fluctuations in regions of the image, where only uncorrelated background is present. This would render the relevant features indiscernible. Fig. ?? shows simultaneously recorded fluorescence intensity (a) and lifetime (b) images. Each fluorescence spot in (a) corresponds to a single chromophore. Some fluorescence spots in (a) are partially cut off due to discrete photobleaching. In the lifetime image (b), only those pixels of the image are displayed, for which the fluorescence intensity in (a) significantly exceeds the background count rate. This is commonly done in lifetime imaging, since the signal shows excessive fluctuations in low count-rate regions of the image, rendering the relevant features indiscernible. In image (a), two fluorescent spots of roughly equal intensity are prominent. Inspection of image (b) shows clearly distinct lifetimes for

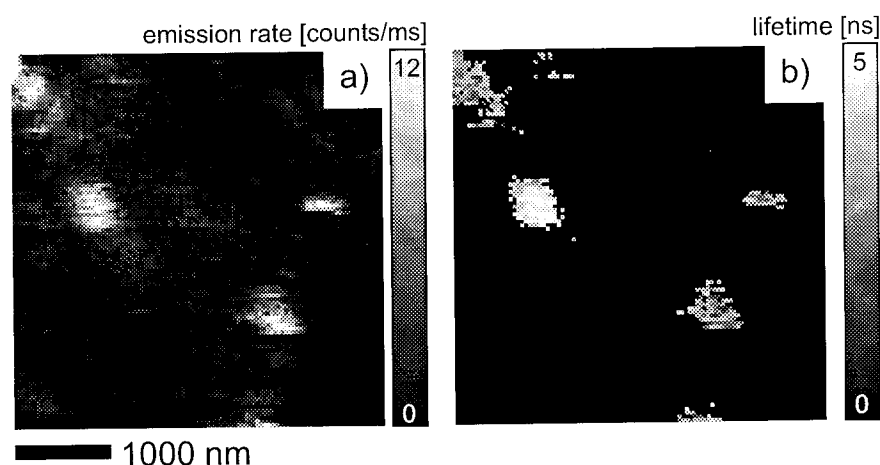


Figure 6.4: Simultaneously acquired fluorescence intensity image (a) and lifetime image (b). Image (a) shows single-molecule spots with varying fluorescence intensities and single-step photobleaching (top-to bottom scan). Image (b) only shows pixels for which the intensity in (a) exceeded a preselected threshold. All other pixels are black. Different lifetimes found for the single-molecule spots are indicated by gray levels.

the two fluorescence spots. It is expected that the lifetime values of single molecules embedded in thin polymer films differ to some extent from the bulk values due to the nearby air-polymer interface [71]. Depending on the relative orientation of the molecule to the interface, the total power that can be radiated by the molecule varies because the nonradiative field components around the molecular dipole interact with the interface. This gives rise to modified fluorescence lifetimes. While molecules with emission dipole moments coplanar to the boundary exhibit lifetimes close to 2 ns, orthogonal orientation results in values around 5 ns. This difference is clearly resolved by our electronics, as seen in Fig. ??.

## 6.5 Conclusions

A novel approach for online determination of fluorescence lifetimes, which is especially well-suited for application at low count-rates, has been introduced. Lifetime imaging of individual molecules provides the experimental proof for reliable opera-

---

tion at low count rates. The method has a strong potential in fluorescence lifetime imaging and application to high-throughput analyses.



# 7. Fluorescence Lifetime of Molecules in Complex Surroundings

Single molecules in complex surroundings can experience marked changes of their fluorescence intensity and lifetime due to nonradiative energy transfer processes. In this chapter it will be shown that variations of the fluorescence lifetime can be obtained by evaluation of the electric field for a specific geometry at the position of the oscillating dipole. As a simplified model for the experiment described in chapter 8, the fluorescence lifetime variations for a molecule embedded in a thin polymer layer on glass are calculated. The latter is separated from a gold halfspace by a small air gap.

## 7.1 Introduction

Molecules, which are embedded in complex surroundings, can experience distinct variations of the fluorescence lifetime. From an electrodynamic point of view, the fluorescence lifetime  $\tau$  of a molecule is defined by the rate  $\gamma = \tau^{-1}$ , at which the molecule dissipates energy to its surroundings. For a dissipated power  $P$  emitted at a frequency  $\omega$ ,  $\tau$  is thus

$$\tau = \frac{\hbar\omega}{P} \quad (7.1)$$

The total radiated power  $P_0$  for a molecule in a homogeneous environment can be obtained as a surface integral over the time-averaged Poynting vector on the boundary  $\partial V$  of a volume  $V$  enclosing the dipolar emitter:

$$P_0 = \int_{\partial V} \langle \mathbf{S} \rangle \cdot \mathbf{n} \, da = \frac{p^2}{12\pi} \frac{\omega}{\epsilon_0 \epsilon} k^3. \quad (7.2)$$

Poynting's theorem, which is essentially a continuity equation for the power flux density [72], states that an alternative way of obtaining the dissipated power  $P_0$  is to integrate over the inner product of current density,  $\mathbf{j}$  and electric field  $\mathbf{E}$ , inside the volume of interest,  $V$ :

$$P_0 = \frac{dW}{dt} = -\frac{1}{2} \int_V \text{Re}(\mathbf{j}^* \cdot \mathbf{E}) dV \quad (7.3)$$

consistent with eq.7.2. Since the current density for an isolated dipole located at  $\mathbf{r}_0$  is represented by a Dirac- $\delta$  function  $\mathbf{j}(\mathbf{r}) = -i\omega \mathbf{p} \delta(\mathbf{r} - \mathbf{r}_0)$ , the above integral 7.3 is evaluated easily:

$$P_0 = \frac{dW}{dt} = \frac{\omega}{2} \text{Im}(\mathbf{p}^* \cdot \mathbf{E}(\mathbf{r}_0)) = \frac{p^2}{12\pi} \frac{\omega}{\epsilon_0 \epsilon} k^3 \quad (7.4)$$

The use of Poynting's theorem has the important advantage that the calculation of the dissipated power is possible, only by knowing the electric field at the location  $\mathbf{r}_0$  of the dipole itself. This result constitutes an essential simplification of the theoretical treatment for complex geometries, when scattered fields have to be considered in addition to the unperturbed dipole field.



For dipoles in an inhomogeneous environment, the following ansatz can be made, dividing the total field into a contribution for the unperturbed dipole,  $\mathbf{E}_0$ , and for the scattered field,  $\mathbf{E}_s$ , at the position  $\mathbf{r}_0$  of the dipole:

$$\mathbf{E}(\mathbf{r}_0) = \mathbf{E}_0(\mathbf{r}_0) + \mathbf{E}_s(\mathbf{r}_0) \quad (7.5)$$

Accordingly, the total radiated power  $P_{\text{tot}}$  is composed of two contributions,  $P_0$ , and  $P_s$ :

$$\begin{aligned} P_{\text{tot}} = P_0 + P_s &= \frac{dW}{dt} = \frac{\omega}{2} \text{Im}(\mathbf{p}^* \cdot (\mathbf{E}_0(\mathbf{r}_0) + \mathbf{E}_s(\mathbf{r}_0))) \\ &= \frac{\omega}{2} \text{Im}(\mathbf{p}^* \cdot \mathbf{E}_0(\mathbf{r}_0)) + \frac{\omega}{2} \text{Im}(\mathbf{p}^* \cdot \mathbf{E}_s(\mathbf{r}_0)) \end{aligned} \quad (7.6)$$

Normalization by  $P_0$  yields

$$\frac{P_{\text{tot}}}{P_0} = 1 + \frac{6\pi\epsilon_0\epsilon}{p^2} \frac{1}{k^3} \text{Im}(\mathbf{p}^* \cdot \mathbf{E}_s(\mathbf{r}_0)) \quad (7.7)$$

With eq. 7.1, the fluorescence lifetime  $\tau$  is obtained:

$$\tau = \tau_0 \left( \frac{P_{\text{tot}}}{P_0} \right)^{-1} \quad (7.8)$$

## 7.2 Theory

In order to calculate  $\tau$  for a specific geometry,  $\mathbf{E}_s$  has to be known at the location of the molecule. The derivation outlined in this section closely follows ref. [73]. The general solution to an electromagnetic boundary value problem for linear, lossless media is found by solving the vectorial Helmholtz equation:

$$(\nabla^2 + k^2)\mathbf{\Pi}(\mathbf{r}) = 0 \quad (7.9)$$

where  $\mathbf{\Pi}$  is the so-called Hertz vector and  $k = (\omega/c)\sqrt{\epsilon\mu}$ ,  $\omega$  being the angular frequency of the electric field,  $c$  the speed of light,  $\epsilon$  the relative dielectric constant and  $\mu$  the relative magnetic permeability. The electric fields and magnetic fields can

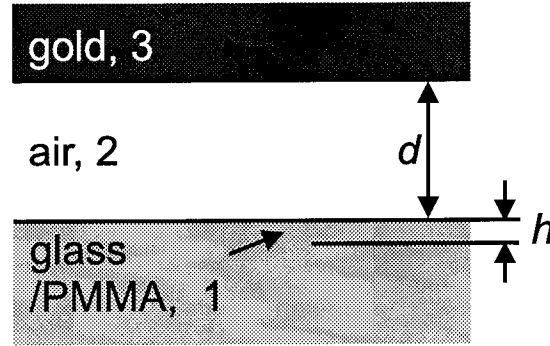


Figure 7.1: Geometry used for the derivation of fluorescence lifetimes. An individual oscillating dipole is placed at a distance  $h$  below the surface of a PMMA layer spin-coated onto a glass substrate (both PMMA and glass are of virtually equal refractive index). A gold mirror is positioned at a distance  $d$  above the glass substrate. The indices 1,2 and 3 are used for the media glass, air and gold, respectively.

be found from

$$\mathbf{E} = (k^2 + \nabla\nabla\cdot)\mathbf{\Pi}(\mathbf{r}) \quad (7.10)$$

$$\mathbf{H} = -i\omega\epsilon_0\epsilon\nabla \times \mathbf{\Pi} \quad (7.11)$$

For a dipole at position  $\mathbf{r}_0$ , the Hertz vector is:

$$\mathbf{\Pi}(\mathbf{r}) = \frac{\mathbf{p}_0}{4\pi\epsilon_0\epsilon} \frac{\exp(ik|\mathbf{r} - \mathbf{r}_0|)}{|\mathbf{r} - \mathbf{r}_0|} \quad (7.12)$$

Due to rotational symmetry, the problem is best treated in cylindrical coordinates, for which the set of basis functions is given by:

$$J_n(k_\rho\rho)\exp(ik_z z + in\varphi) \quad (7.13)$$

where the orthogonal radial  $k_\rho$  and  $z$ -component  $k_z$  of the wavenumber are inter-related by  $k^2 = k_\rho^2 + k_z^2$ , and  $J_n$  is the Bessel function of  $n$ th order. In order to express eq. 7.12 in terms of the cylindrical basis functions 7.13, an identity derived by Sommerfeld has to be used:

$$\frac{\exp(ikR_0)}{R_0} = i \int_0^\infty dk_\rho \frac{k_\rho}{k_z} J_0(k_\rho\rho)\exp(ik_z|z - h|) \quad (7.14)$$

where  $R_0 = |\mathbf{r} - \mathbf{r}_0|$ . The geometry used for the present derivation is depicted in Fig. 7.1. A single emitting dipole is embedded at a small distance  $h$  below the surface of a thin polymer film deposited onto a glass substrate. The relative dielectric constants  $\epsilon$  are virtually equal for the glass substrate and the polymer layer. An air gap of width  $d$  separates the polymer film from a gold-halfspace. The relative dielectric constants in the media 1, 2 and 3 are denoted as  $\epsilon_1$ ,  $\epsilon_2$ , and  $\epsilon_3$ , respectively.

Using eq. 7.14 and eq. 7.2, an ansatz for  $\mathbf{\Pi}$  can be made for all three layers. As an example, the expression for  $\mathbf{\Pi}$  in medium 2, for a vertically oriented dipole, reads as:

$$\mathbf{\Pi}_{2,z} = \frac{p_{0,z}}{4\pi\epsilon_0\epsilon} \int_0^\infty dk_\rho J_0(k_\rho\rho) \exp(-ik_{2,z}h) * [A_2(k_\rho) * \exp(ik_{2,z}z) + B_2(k_\rho) * \exp(-ik_{2,z}z)] \quad (7.15)$$

Eq. 7.15 is an expansion of the kind 7.14, where  $A_2$  are the amplitudes of plane waves propagating in the upward direction and  $B_2$  for the downward direction, correspondingly. For regions 1 and 3, an analogous ansatz is made, setting  $B_3$  and  $A_1$  to zero, because of the absence of incoming waves in the media 1 and 3 and including a dipolar source term in medium 1. The coefficients  $A_i$  and  $B_i$  are determined by the boundary condition, which states that the tangential components of both  $\mathbf{E}$  and  $\mathbf{H}$  have to be continuous across the interfaces.

For obtaining  $\tau$ ,  $\mathbf{E}(\mathbf{r}_0)$  is calculated from  $\mathbf{\Pi}$  and inserted into eq. 7.6. Explicit expressions for the field are given in ref. [73].

## 7.3 Results and Discussion

In Fig. 7.2, the fluorescence lifetime relative to its value in a homogeneous polymeric medium of dielectric constant  $\epsilon_1$  is plotted as a function of the gapwidth  $d$ . At large separations, weak modulations on top of a constant value are observed, due to slight modifications of the radiative decay rate. The latter result from changes of the number of modes available for photon emission in the cavity between the glass substrate and the gold mirror. Interestingly, the lifetime does not converge

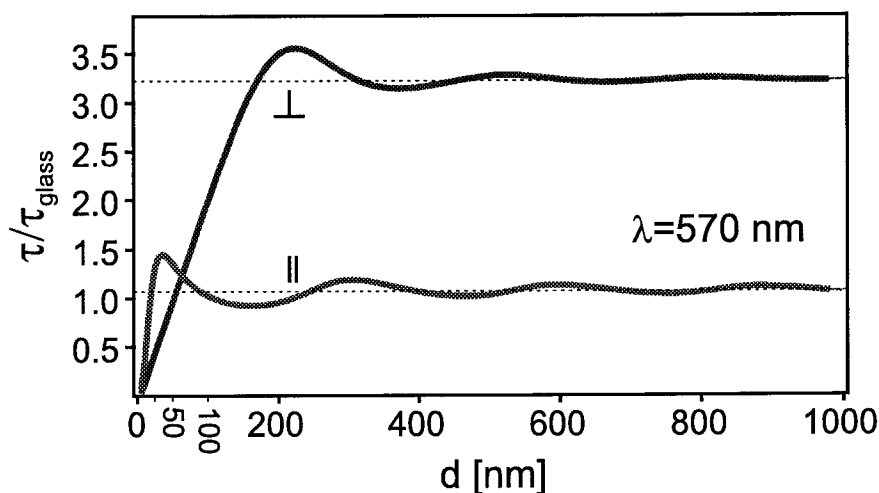


Figure 7.2: Variation of the normalized lifetime  $\tau/\tau_0$  as a function of the spacing between the gold mirror and the glass substrate. The wavelength of emission was chosen to be  $\lambda = 570 \text{ nm}$ , as is the case for the fluorescence dye DiI.  $\perp$  indicates the case, where the molecular emission dipole is orthogonal to the substrate surface,  $\parallel$  the parallel case.

accurately towards its free-space value for either the perpendicular ( $\perp$ ) or the parallel ( $\parallel$ ) case. This effect results from the close proximity between the molecule and the PMMA/air interface [71].

At small spacings of mirror and PMMA/air-interface, dramatic shortening of the fluorescence lifetime sets in. The latter results from efficient nonradiative transfer of molecular excitation energy to the metallic mirror. In order to quantify the range of interaction of nonradiative energy transfer, the distance, at which  $\tau/\tau_0 = 0.5$ , is taken as a measure. For the orientation  $\perp$ , this distance is in the 25 nm range. For the case  $\parallel$ , it is even on the order of 10 nm. In a simple physical picture, the oscillating molecular dipole drives electrons within the metal, thereby dissipating energy. Another possible source of nonfluorescent energy loss is the excitation of propagating waves (e.g. plasmons) on the metallic mirror, which effectively drain energy from the dipole.

It is important to note that the fluorescence lifetime shortening, which arises at small molecule-metal spacings, does *not* give rise to enhanced fluorescence, since it

is induced by an increase of the nonradiative decay rate  $k_{nr}$ . For this reason, the fluorescence quantum yield  $\phi_f = k_r/(k_r + k_{nr})$  drops simultaneously.

## 7.4 Experimental Relevance

In chapter 8, a metallized scanning probe microscopy tip is used for perturbing a fluorescence molecule embedded in a thin polymer film. With regard to a possible comparison between the analytical results obtained in this chapter and the experiments, which were conducted for a different geometry, the range of validity of the planar model should be discussed.

Fig. 7.2 shows, that pronounced effects of the metallic surface on the molecules set in at very small distances in the 10-20 nm range. For the employed  $Si_3N_4$  tips, the radii of curvature are not below 20 nm. Taking into account that a layer of 50 nm of gold was evaporated onto the tip, an effective radius of curvature of  $\approx 70nm$  is expected, hence the tip can be viewed as a plane surface on the relevant length scale of 20 nm. For the experiment discussed in 8, it is expected that the dipolar nature of emitting molecules should give rise to orientation-dependent patterns in the lifetime map. However, in the frame of the model, no predictions can be made for such patterns, since for an infinitely extended gold mirror, for symmetry reasons, no change is expected upon lateral displacements. Information about the lifetime variation during a z-scan of the tip is in principle contained in the scan images, since the sidefaces of the pyramidal tip change their distance to the molecule during lateral tip scans.



## 8. Single-molecule near-field optical energy transfer microscopy

In this chapter, a novel near-field optical contrast mechanism based on the local enhancement of *radiationless* decay of a single fluorescent molecule by a sharp metallic probe tip is demonstrated. In this type of experiment, both, field enhancement and fluorescence quenching, can give rise to a change in fluorescence emission. In order to identify quenching processes, fluorescence intensity *and* lifetime are mapped simultaneously, while scanning a metallized tip across a molecule. The observation of a local decrease in fluorescence intensity *together* with a shortening of the excited state lifetime proves unambiguously that the vicinity of the tip opens up additional decay channels for the molecule.

## 8.1 Introduction

Scanning near-field optical microscopy (SNOM) is an optical imaging technique that overcomes the limits of diffraction by requiring subwavelength proximity between an optical probe and a sample. Aperture SNOM [6, 74] has been successfully used to demonstrate the potential of near-field optical (NFO) techniques in various applications ranging from ultra-high density data storage [75] to super-resolution imaging of single fluorescent molecules [10, 76]. However, the application of these techniques is complicated by the difficult fabrication and the low light throughput of aperture probes. Tip-enhanced techniques constitute an alternative approach to NFO imaging. Tip-enhanced SNOM has been applied to image polymer mixtures with infrared light in vibrational absorption at a resolution of  $\lambda/100$  [77]. In the visible spectrum tip-enhanced two-photon fluorescence microscopy [78] and tip-enhanced fluorescence [79–82] have been discussed. In spite of these achievements, no tip-enhanced NFO scheme with single-molecule sensitivity has been introduced yet.

Quenching of the sample's fluorescence by the proximity of the metallic probe tip is thought to be a major disadvantage of tip-enhanced SNOM techniques. Here, it will be shown that local fluorescence quenching [83] and lifetime changes [84, 85] due to the proximity of a metallized tip can be advantageously used as a contrast mechanism in SNOM with single-molecule sensitivity. For demonstration of the approach, single molecules embedded in a thin polymer film are scanned by a metallized AFM tip. Maps of fluorescence intensity and lifetime as a function of tip position show features of a size well below the diffraction limit. The lifetime map clearly demonstrates a shortened lifetime, compatible with the presence of a quenching effect.

## 8.2 Experimental

Fig. 8.1 shows the experimental setup employed in the present study. It consists of a scanning confocal optical microscope based on an inverted microscope (Zeiss Axiovert 135) onto which an atomic force microscope (AFM) (Digital Instruments, Bioscope) is mounted. An actively mode-locked Nd:YAG laser (Coherent Antares),



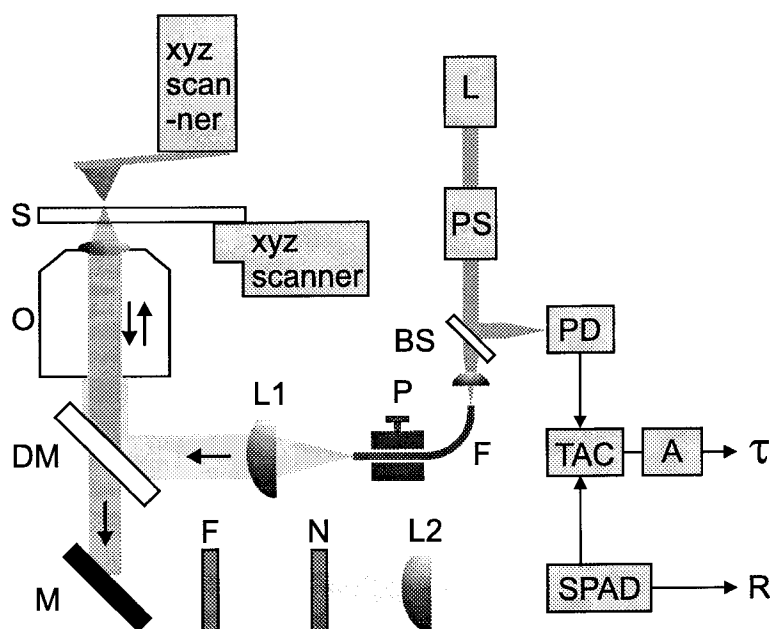


Figure 8.1: Experimental setup. L: laser, PS: power stabilizer, BS: beam-splitter, PD: photodiode, F: optical fiber, P: polarization controller, L1, L2: lenses, DM: dichroic mirror, O: objective, S: sample, M: mirror, F: filter, N: notch filter, SPAD: single-photon counting avalanche diode, TAC: time-to-amplitude converter, A: averaging unit; outputs: R: fluorescence count rate,  $\tau$ : fluorescence lifetime signal.

frequency-doubled to 532 nm, was used as a light source that delivers 150 ps wide pulses with a repetition rate of 76 MHz. A beam-splitter directs a small fraction of the excitation laser light towards a fast PIN-photodiode in order to provide a time reference for measuring excited state lifetimes. A power stabilizer (PS) (Cambridge Instruments, LS 100) is used for reducing fluctuations of the average laser intensity to about 1 percent of the total intensity. Spatial filtering of the laser beam is provided by coupling the light into a single-mode fiber. A commercial device (L.O.T. Polarite) allows for polarization control by mechanically introducing birefringence in the optical fiber. At the exit of the fiber, the light is collimated by a lens L1 and reflected via a dichroic mirror onto the entrance aperture of an immersion oil microscope objective (Zeiss, Plan-Apochromat, x63, 1.4 NA,  $\infty$ ) which focuses the light to a diffraction limited spot on the sample. Fluorescence is collected by the objective, filtered by the dichroic mirror and a holographic notch filter for suppression of backscattered excitation laser light, and focused onto the active area of a single-photon counting avalanche photodiode (SPAD) (SPCM-ARQ 14, Perkin-Elmer). An additional notch-filter and a shortpass filter were inserted into

the optical path to guarantee that the laser light employed for position feedback of the AFM ( $\lambda = 675 \text{ nm}$ ) is effectively filtered out. The  $200 \mu\text{m}$  diam. active area of the SPAD serves as a confocal pinhole. The SPAD's TTL output is directly fed into a counter that is integrated into the AFM electronics. Samples were prepared by spincoating (9600 rpm) of a  $10 \mu\text{l}$  droplet of a solution of polymethylmetacrylate (PMMA) in toluene that contained the dye *1,1'-dioctadecyl-3,3,3',3'-tetramethylindocarbocyanine* (DiI) at a concentration of  $\approx 10^{-9} \text{ M}$  onto standard glass cover slips. The cover slips were cleaned by baking them at  $510^\circ\text{C}$  for six hours. The refractive indices of PMMA and glass are virtually equal. Atomic force microscopy of the polymer film revealed a smooth surface and a thickness of about  $30 \text{ nm}$ . Standard single-molecule fluorescence images acquired by sample-scanning SCOM without a mounted AFM tip showed typical circular diffraction-limited fluorescence spots of a full width at half maximum of  $250 \text{ nm}$ . For online acquisition of lifetime data during scans, the circuit described in chapter 6 is used. Its output voltage is fed into an ADC channel of the AFM to obtain lifetime maps as a function of the tip-position.

### 8.3 Alignment Procedure

Prior to an experiment, proper alignment of the AFM tip with respect to the optical axis of the setup has to be achieved, i.e. the apex of the tip has to be positioned within or very close to the confocal volume. This is achieved by tilting the notch filter until it becomes partially transmissive and recording backscattered light as a function of the tip position (tip scan). In this configuration, reflection of excitation light occurs both at the polymer-air interface and at the metallized cantilever. These two back-reflected components give rise to interferences, as a function of tip position. In order to observe the weak modulations, a power stabilizer has to be used because laser intensity fluctuations can easily obscure this pattern. Fig. 8.2 shows a reflection-mode image of a cantilever obtained by a large-range tip scan. At the end of the roughly triangular lever, the pyramidal AFM probe can be seen. The apex region of the probe is seen as a spot of enhanced reflectivity. After zooming in to a  $1 \times 1 \mu\text{m}^2$  region around this point, the notch filter is tilted back to the initial position in order to record fluorescence. The tip is now fixed. An actively linearized

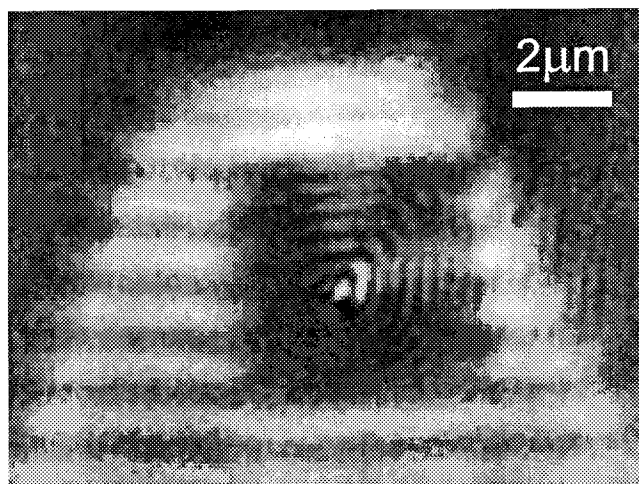


Figure 8.2: Image of the AFM cantilever, as obtained in reflection-mode SCOM, when scanning the cantilever across the confocal volume. The interference fringes indicate the shape of the pyramidal tip. The tip apex is seen as a spot of strong reflection.

piezoelectric xyz-scanning stage (PI, model E-500) is used for sample positioning. For locating molecules, the sample is scanned manually, until the fluorescence count rate significantly exceeds the background rate, indicating the presence of a molecule within the confocal volume. Once a molecule has been found, the position of the scan stage is kept fixed, for continuous monitoring of the molecular fluorescence (excitation intensity: 500 nW, typical emission rates: 10-20 kHz).

## 8.4 Results and Discussion

Fig. 8.3 shows a typical map of fluorescence intensity obtained during a top to bottom tip-scan. At the top of the image, constant fluorescence intensity is observed, which persists for several scan lines, until the count-rate drops to background, due to sudden photodestruction of the molecule. The subsequent darker streak corresponds to the time required for manually selecting a new molecule. The second molecule stays stable throughout the scanning process until finally, at the bottom of the image, irreversible photobleaching occurs. A further characteristic single-molecule feature is the occurrence of brief non-emissive periods throughout the image, which

are seen as short dark streaks. These dark periods are due to excursions of the molecule to the triplet state.

Those parts of the image that represent molecular fluorescence, clearly exhibit fringe-like patterns, with a pronounced local decrease of fluorescence intensity at their center. The fringes are most likely of a far-field origin, as suggested by their period, which is comparable with the wavelength of illumination light. We ascribe their occurrence to the presence of the AFM probe, which is a pyramid of a base length of 4  $\mu m$  and a height of 3.3  $\mu m$ . In AFM scans, only the tip apex interacts with the sample. In fluorescence experiments, also the regions of the tip, which are not in immediate contact with the sample, affect image formation. Depending on the position offset between molecule and tip, the molecule experiences an effectively increased or decreased excitation intensity due to reflection of excitation laser light by the tip. Another possible cause for a modified excitation field is the so-called lightning rod effect. It occurs for tip shapes with radii of curvature, which are much smaller than the excitation wavelength, when the incident illumination field is polarized along the long axis of the tip. In the present case, however, fluorescence quenching seems to be the dominant effect, since no local enhancement is observed.

In contrast to the far-field fringes described above, the sharp local decrease at the center of the intensity map is clearly of subdiffraction-limited dimensions, indicating a near-field optical origin, presumably due to quenching of the molecular fluorescence by the tip. It exhibits a double-lobed shape. In principle, double-lobed shapes would be expected for dipolar emitters, indicating their orientation. However, images acquired on several molecules (with random orientations) with one and the same tip exhibit identically oriented double-lobe patterns. The shape of the patterns is therefore most likely due to an asymmetry of the tip. A line-cut across the upper lobe reveals a width of 70 nm and a local decrease of the fluorescence count rate by 10 kHz, with steep edges, indicative of very short-ranged interactions. In the lower lobe, which is spatially more extended, almost complete suppression of the molecular fluorescence down to a count rate of 5 kHz is seen.

The fluorescence intensity map alone does not permit to conclude, whether a change in the emission rate of a molecule stems from an altered excitation field or from

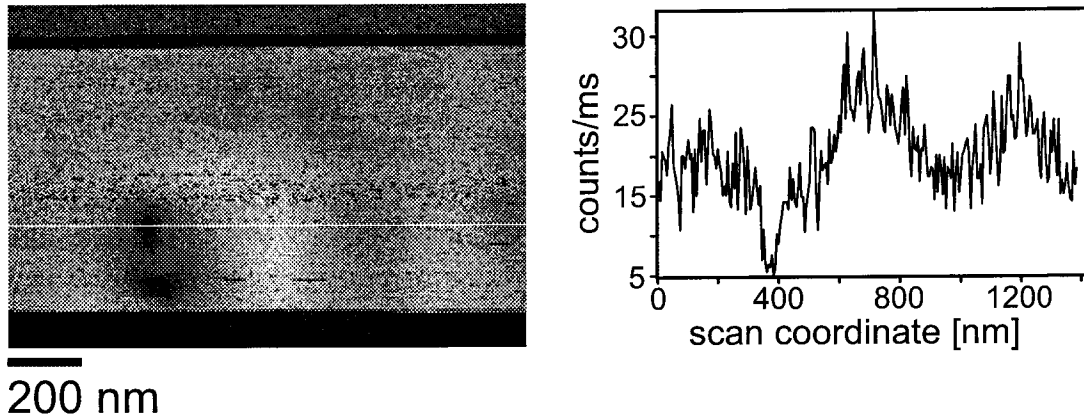


Figure 8.3: Left side: Map of fluorescence intensity as a function of the relative offset between molecule and tip. Fringe patterns around the central dip are due to reflection of excitation light on the cantilever, as is obvious from their length scale ( $\approx \lambda/2$ ). Right side: linesection of the intensity map along the white line seen in the left image. The lateral extension of the dip of 70 nm indicates a near-field origin.

opening up new decay channels. For this reason, simultaneous fluorescence lifetime mapping has been performed.

In chapter 2, it was shown that changes of the nonradiative rate constant  $k_{nr}$  are manifested in modified fluorescence lifetimes. Continuous monitoring of the fluorescence lifetime therefore provides a measure for the strength of the nonradiative energy transfer from the excited state of the molecule into the metal, i.e. quenching. In figure 8.4, a map of the fluorescence lifetime is shown, which was recorded simultaneously with the fluorescence map. The lifetime map reproduces the subdiffraction-limited dip, while the fringes are not visible. This underscores the above stated assumption that the fringes do not result from genuine near-field interactions. The dip appears at the same position in the image, and is 70 nm in width, in consistence with the dip in figure 8.3. Its depth corresponds to a local lifetime decrease of more than 1 ns. The comparison of figs. 8.3 and 8.4 reveals two important findings:

1. Fringe-like patterns are observed for the fluorescence intensity map, without a counterpart in the lifetime map
2. At the center of the fringes, a strong local decrease of fluorescence is seen in the intensity map. At the coincident position, the lifetime map exhibits a local decrease.

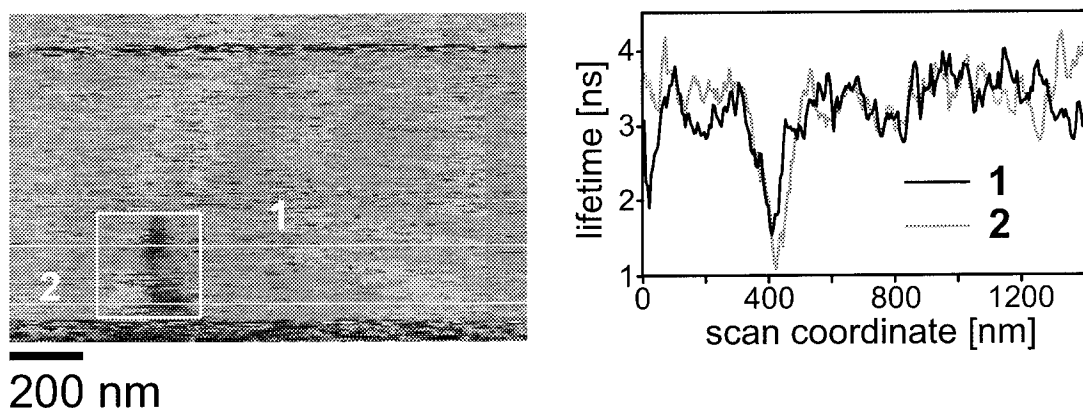


Figure 8.4: Left image: Fluorescence lifetime map for the scan shown in Fig. 8.4. The fluorescence remains constant, until the AFM tip comes into close proximity of the molecule. The position of the feature is coincident with the central dip in Fig. 8.4. Right image: Linesection across the feature, as indicated in the left image. A local decrease of the fluorescence lifetime by more than 1 ns with a width of 70 nm is seen.

With regard to the photophysics of molecules, as discussed in chapter 2, the interpretation of the effects becomes clear:

Variations of the excitation intensity  $I$  affect the rate of excitation  $k_{12} = \sigma I$ , which is linearly translated into the emission rate  $R(I)$ , provided that the molecule is not in saturation. Changes in  $R(I)$  do not result in an altered lifetime. Dissipation of excitation energy into the metal gives rise to an increase of  $k_{nr}$ , which has two consequences: The lifetime  $\tau$  is lowered, according to  $\tau^{-1} = k_r + k_{nr}$ . At the same time, the fluorescence quantum yield  $\phi_f = \frac{k_r}{k_r + k_{nr}}$  drops. Simultaneously occurring decreases of the fluorescence count-rate *and* fluorescence intensity therefore reflect the presence of nonradiative decay channels for the molecule.

## 8.5 Experiments with uncoated $Si_3N_4$ tips

In order to assess the effect of dielectric objects in the vicinity of fluorescent molecules, the experiments described above were also conducted with uncoated  $Si_3N_4$  tips. Unexpectedly, both the intensity map (Fig. 8.5) and the lifetime map (Fig. 8.6) show a modulation comparable to the results obtained with the metallic tip. This is surprising, since strong dissipation of energy is not expected for dielec-

tric media, such as  $Si_3N_4$ . An alternative pathway, which can give rise to lowering of the measured excited state lifetime, is the conversion of the nonradiative near-field of the molecule into radiating fields by the transparent  $Si_3N_4$  tip. Due to the

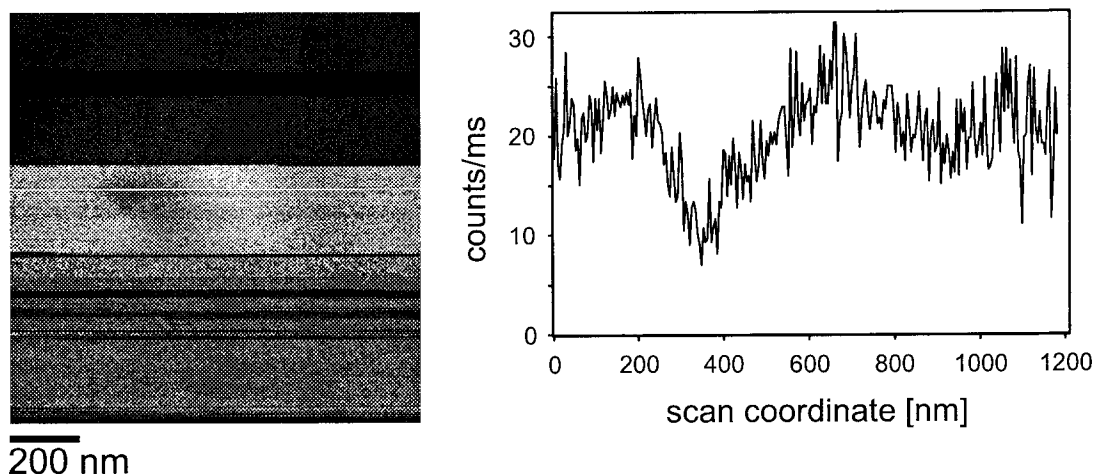


Figure 8.5: Left image: Fluorescence intensity map obtained with a  $Si_3N_4$  tip. Right image: Linescans across the feature, as indicated in the left image. A local decrease of the fluorescence count rate by 10 kHz with a width of 150 nm is observed.

very high refractive index of  $Si_3N_4$  ( $n=1.8$ ), very efficient coupling of the molecular near-field to the tip can be expected. In the silicon nitride material, photons can propagate and thus be guided away effectively into the upper halfspace, where they are not detected. In the frame of the rate equation model of chapter 2, this tapping of the near-field is equivalent to a radiationless decay channel of the molecule, and thus leads to a shortening of the fluorescence lifetime and a decrease of the detected fluorescence.

## 8.6 Conclusion

It was shown that significant fluorescence lifetime changes arise, when metallic or dielectric objects are approached to fluorescent molecules. In both cases, the perturbing object provides additional decay channels for the molecule. In the case of metallic objects it was concluded that nonradiative dissipation of molecular excitation energy is responsible for the lifetime shortening. For dielectric perturbors, the lifetime is shortened due to the conversion of nonradiative near-fields to propagating

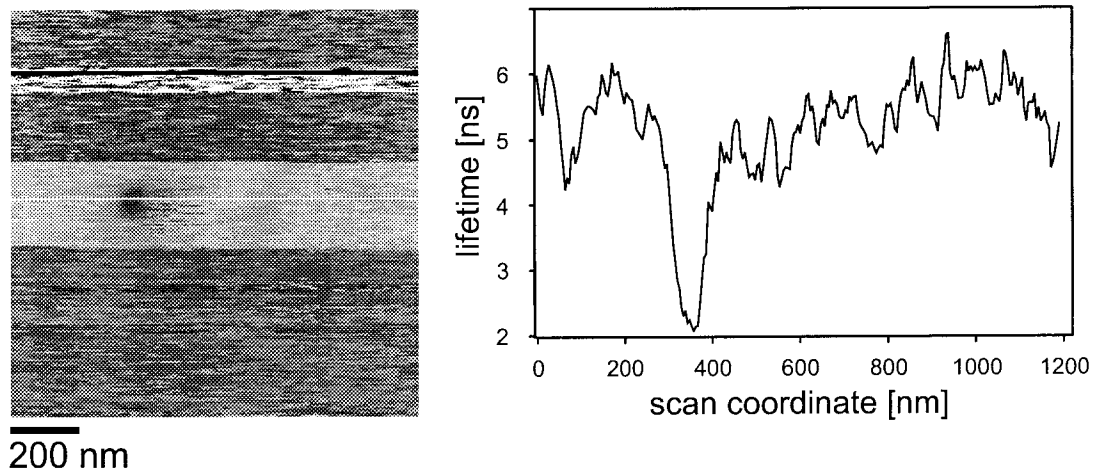


Figure 8.6: Left image: Fluorescence lifetime map obtained with a  $Si_3N_4$  tip. Right image: Linesection across the feature, as indicated by the white line in the left image. A local decrease of the fluorescence lifetime down to 2 ns with a width of 150 nm is observed.

modes in the tip, which radiate into solid angles, where the light is not detected. Very short-ranged interactions have been observed, which could be exploited for NFO imaging. The suggested method further holds promise to allow systematic investigations on the origin of optical contrast in tip-enhanced NFO imaging methods.



# Bibliography

- [1] R. Descartes, *Discours de la methode*.
- [2] M. Knoll and E. Ruska, "Das Elektronenmikroskop," *Z. Physik* **78**, 318–339 (1932).
- [3] G. Binnig, H. Rohrer, C. Gerber, and E. Weibel, "Surface Studies by Scanning Tunneling Microscopy," *Phys. Rev. Lett.* **49**, 57 (1982).
- [4] G. Binnig, C. Quate, and C. Gerber, "Atomic Force Microscope," *Phys. Rev. Lett.* **56**, 930 (1986).
- [5] W. Moerner and L. Kador, "Optical Detection and Spectroscopy of Individual Molecules in a Solid," *Phys. Rev. Lett.* **62**, 2535 (1989).
- [6] D. Pohl, W. Denk, and M. Lanz, "Optical Stethoscopy - Image Recording With Resolution  $\lambda/20$ ," *Appl. Phys. Lett.* **44**, 651–653 (1984).
- [7] T. Basche, W. Moerner, M. Orrit, and H. Talon, "Photon Antibunching in the Fluorescence of a Single Dye Molecule Trapped in a Solid," *Phys. Rev. Lett.* **69**, 1516–1519 (1992).
- [8] E. Betzig and R. J. Chichester, "Single Molecules Observed by Near-Field Scanning Optical Microscopy," *Science* **262**, 1422–1425 (1993).
- [9] T. Ha, J. Glass, T. Enderle, D. S. Chemla, and S. Weiss, "Hindered Rotational Diffusion and Rotational Jumps of Single Molecules," *Phys. Rev. Lett.* **80**, 2093–2096 (1998).
- [10] M. A. Bopp, A. J. Meixner, G. Tarrach, I. Zschokke-Granacher, and L. Novotny, "Direct Imaging Single Molecule Diffusion in a Solid Polymer Host," *Chem. Phys. Lett.* **263**, 721–726 (1996).
- [11] S. Weiss, "Fluorescence Spectroscopy of Single Biomolecules," *Science* **283**, 1676–1683 (1999).

- [12] L. Fleury, J. Segura, G. Zumofen, B. Hecht, and U. Wild, "Nonclassical Photon Statistics in Single-Molecule Fluorescence at Room Temperature," *Phys. Rev. Lett.* **84**, 1148–1151 (2000).
- [13] M. Orrit and J. Bernard, "Single Pentacene Molecules detected by fluorescence excitation in a p-terphenyl crystal," *Phys. Rev. Lett.* **65**, 2716–2719 (1990).
- [14] L. Fleury, J. Segura, G. Zumofen, B. Hecht, and U. Wild, "Single-Molecule Spectroscopy-Stark Effect of Pentacene in Para-Terphenyl," *Chem. Phys. Lett.* **193**, 451–455 (1992).
- [15] T. Basché, W. E. Moerner, M. Orrit, and U. P. Wild, *Single-molecule optical detection, imaging and spectroscopy* (VCH, Weinheim, 1997).
- [16] J. J. Macklin, J. K. Trautman, T. D. Harris, and L. E. Brus, "Imaging and Time-Resolved Spectroscopy of Single Molecules at an Interface," *Science* **272**, 255–258 (1996).
- [17] S. Nie, D. T. Chiu, and R. N. Zare, "Probing Individual Molecules with Confocal Fluorescence Microscopy," *Science* **266**, 1018–1021 (1994).
- [18] R. Vale, T. Funatsu, D. Pierce, L. Romberg, Y. Harada, and T. Yanagida, "Direct Observation of Single Kinesin Molecules Moving Along Microtubules," *Nature* **380**, 451–453 (1996).
- [19] R. M. Dickson, D. J. Norris, Y. L. Tzeng, and W. E. Moerner, "Three-Dimensional Imaging of Single Molecules Solvated in Pores of poly(acrylamide) Gels," *Science* **274**, 966–969 (1996).
- [20] H. P. Lu, L. Xun, and X. S. Xie, "Single-Molecule Enzymatic Dynamics," *Science* **282**, 1877–1882 (1998).
- [21] T. Schmidt, G. J. Schütz, H. J. Gruber, and H. Schindler, "Local Stoichiometries Determined by Counting Individual Molecules," *Anal. Chem.* **68**, 4397–4401 (1996).
- [22] A. Papoulis, *Probability, Random Variables, and Stochastic Processes* (McGraw-Hill, New York, 1992).
- [23] N. Bobroff, "Position Measurement with a Resolution and Noise-Limited Instrument," *Rev. Sci. Inst.* **57**, 1152–1157 (1986).
- [24] T. Schmidt, G. Schütz, H. Gruber, and H. Schindler, "Local Stoichiometries Determined by Counting Individual Molecules," *Anal. Chem.* **68**, 4397–4401 (1996).

- [25] L. A. Utracki, *Polymer alloys and blends: Thermodynamics and rheology* (Carl Hanser Verlag, München, 1989).
- [26] H. Vestweber, A. Greiner, U. Lemmer, R. Mahrt, R. Richert, W. Heitz, and H. Bässler, "Progress Towards Processible Materials For Light-Emitting Devices using Poly(p-phenylphenylenevinylene)," *Adv. Mater.* **4**, 661-662 (1992).
- [27] M. Granström and O. Inganäs, "White Light Emission from a Polymer Blend Light Emitting Diode," *Appl. Phys. Lett.* **68**, 147-149 (1996).
- [28] C. Weder, C. Sarwa, A. Montali, C. Bastiaansen, and P. Smith, "Incorporation of Photoluminescent Polarizers into Liquid Crystal Displays," *Science* **279**, 835-837 (1998).
- [29] A. Montali, C. Bastiaansen, P. Smith, and C. Weder, "Polarizing Energy Transfer in Photoluminescent Materials for Display Applications," *Nature* **392**, 261-264 (1998).
- [30] J. H. Burroughes, D. D. C. Bradley, A. R. Brown, R. N. Marks, K. Mackay, R. Friend, P. L. Burn, and A. B. Holmes, "Light-Emitting-Diodes based on Conjugated Polymers," *Nature* **347**, 539-541 (1990).
- [31] J. H. Burroughes, C. A. Jones, and R. H. Friend, "New Semiconductor-Device Physics in Polymer Diodes and Transistors," *Nature* **335**, 137-141 (1988).
- [32] V. Tessler, G. J. Denton, and R. Friend, "Lasing From Conjugated-Polymer Microcavities," *Nature* **382**, 695-697 (1996).
- [33] P. J. Flory, *Macromolecules* **11**, 1138 (1978).
- [34] R. Koningsveld, W. H. Stockmayer, and E. Nies, *Polymer Phase Diagrams* (Oxford University Press, in press).
- [35] M. B. Gieselman and J. R. Reynolds, "poly(para-phenyleneterephthalamido)propanesulfonate) - A New Polyelectrolyte for Application to Conducting Molecular Composites," *Macromolecules* **23**, 3118-3124 (1990).
- [36] U. Lauter, W. H. Meyer, and G. Wegner, "Molecular Composites From Rigid-Rod poly(p-phenylene)s with oligo(oxyethylene) Side Chains as Novel Polymer Electrolytes," *Macromolecules* **30**, 2092-2101 (1997).
- [37] C. D. Eisenbach, J. Hofmann, and K. Fischer, "Blends of Rigid-Rod and Flexible Macromolecules," *Macromol. Rapid. Commun.* **15**, 117-124 (1994).

- [38] D. Wirtz, D. E. Werner, and G. G. Fuller, "Structure and Optical Anisotropies of Critical Polymer-Solutions in Electric-Fields," *J. Chem. Phys.* **101**, 1679–1686 (1994).
- [39] J. van Egmond and G. G. Fuller, "Concentration Fluctuation Enhancement in Polymer-Solutions by Extensional Flow," *Macromolecules* **26**, 7182–7188 (1993).
- [40] C. Weder, C. Sarwa, C. Bastiaansen, and P. Smith, "Highly Polarized Luminescence from Oriented Conjugated Polymer/Polyethylene Blend Films," *Adv. Mater.* **9**, 1035 (1997).
- [41] C. Weder and M. S. Wrighton, "Efficient Solid-State Photoluminescence in New poly(2,5-dialkoxy-p-phenyleneethynylene)s," *Macromolecules* **29**, 5157–5165 (1996).
- [42] T. Ha, T. Enderle, D. S. Chemla, P. R. Selvin, and S. Weiss, "Single Molecule Dynamics Studied by Polarization Modulation," *Phys. Rev. Lett.* **77**, 3979–3982 (1996).
- [43] J. Sepiol, J. Jasny, J. Keller, and U. P. Wild, "Single Molecules Observed by Immersion Mirror Objective. The Orientation of Terrylene Molecules via the Direction of its Transition Dipole Moment," *Chem. Phys. Lett.* **273**, 444–448 (1997).
- [44] T. Ha, J. Glass, T. Enderle, D. Chemla, and S. Weiss, "Hindered Rotational Diffusion and Rotational Jumps of Single Molecules," *Phys. Rev. Lett.* **80**, 2093–2096 (1998).
- [45] R. M. Dickson, D. J. Norris, and W. E. Moerner, "Simultaneous Imaging of Individual Molecules Aligned Both Parallel and Perpendicular to the Optical Axis," *Phys. Rev. Lett.* **81**, 5322–5325 (1998).
- [46] S. A. Empedocles, R. Neuhauser, and M. G. Bawendi, "Three-Dimensional Orientation Measurements of Symmetric Single Chromophores using Polarization Microscopy," *Nature* **399**, 126–130 (1999).
- [47] A. P. Bartko and R. M. Dickson, "Imaging Three-Dimensional Single Molecule Orientations," *J. Phys. Chem. B* **103**, 11237–11241 (1999).
- [48] B. Sick, B. Hecht, and L. Novotny, "Orientational Imaging of Single Molecules by Annular Illumination," *Phys. Rev. Lett.* **85**, 4482–4485 (2000).

- [49] D. A. vanden Bout, W. T. Yip, D. Hu, D. K. Fu, T. Swager, and P. F. Barbara, "Discrete Intensity Jumps and Intramolecular Electronic Energy Transfer in the Spectroscopy of Single Conjugated Polymer Molecules," *Science* **277**, 1074–1077 (1997).
- [50] W. T. Yip, D. Hu, J. Yu, D. A. vanden Bout, and P. F. Barbara, "Classifying the Photophysical Dynamics of Single- and Multiple-Chromophoric Molecules by Single Molecule Spectroscopy," *J. Phys. Chem. A* **102**, 7564–7575 (1998).
- [51] P. R. Bevington and D. K. Robinson, *Data reduction and error analysis for the physical sciences* (McGraw-Hill, New York, 1994).
- [52] A. Mayer and S. Neuenhofer, "Luminescent Labels - More Than Just an Alternative to Radioisotopes," *Angew. Chem. Int. Ed. Engl.* **33**, 1044–1072 (1994).
- [53] T. Förster, "Zwischenmolekulare Energiewanderung und Fluoreszenz," *Ann. Physik* **2**, 55–75 (1947).
- [54] L. Stryer and R. P. Haugland, "Energy Transfer: A Spectroscopic Ruler," *Proc. Natl. Acad. Sci.* **58**, 719–726 (1967).
- [55] A. Castro and J. G. K. Williams, "Single-Molecule Detection of Specific Nucleic Acid Sequences in Unamplified Genomic DNA," *Anal. Chem.* **69**, 3915–3920 (1997).
- [56] U. Kettling, A. Koltermann, P. Schwille, and M. Eigen, "Real-Time Enzyme Kinetics Monitored by Dual-Color Fluorescence Cross-Correlation Spectroscopy," *Proc. Natl. Acad. Sci.* **95**, 1416–1420 (1998).
- [57] "Frontiers in Chemistry: Single Molecules," *Science* 283 (1999).
- [58] M. Eigen and R. Rigler, "Sorting Single Molecules - Application to Diagnostics and Evolutionary Biotechnology," *Proc. Natl. Acad. Sci.* **91**, 5740–5747 (1994).
- [59] R. Rigler, "Fluorescence Correlations, Single-Molecule Detection and Large Number Screening - Applications in Biotechnology," *J. Biotech.* **41**, 177–186 (1995).
- [60] W. Trabesinger, G. Schütz, H. J. Gruber, H. Schindler, and T. Schmidt, "Detection of Individual Oligonucleotide Pairing by Single-Molecule Microscopy," *Anal. Chem.* **71**, 279–283 (1999).
- [61] K. C. Ng, W. B. Whitten, S. Arnold, and J. M. Ramsey, "Digital Chemical Analysis of Dilute Microdroplets," *Anal. Chem.* **64**, 2914–2919 (1992).

- [62] G. J. Schütz, W. Trapesinger, and T. Schmidt, "Direct Observation of Ligand Colocalization on Individual Receptor Molecules," *Biophys. J.* **74**, 2223–2226 (1998).
- [63] E. Betzig, "Proposed Method for Molecular Optical Imaging," *Opt. Lett.* **20**, 237–239 (1995).
- [64] A. M. van Oijen, J. Köhler, J. Schmidt, M. Müller, and G. J. Brakenhoff, "3-Dimensional Super-Resolution by Spectrally Selective Imaging," *Chem. Phys. Lett.* **292**, 183–187 (1998).
- [65] T. D. Lacoste, X. Michalet, F. Pinaud, D. S. Chemla, A. P. Alivisatos, and S. Weiss, "Ultra-high-Resolution Multicolor Colocalization of Single Fluorescent Probes," *Proc. Natl. Acad. Sci.* **97**, 9461–9466 (2000).
- [66] S. Chandrasekhar, "Stochastic Problems in Physics and Astronomy," *Rev. Mod. Phys.* **15**, 1–89 (1943).
- [67] M. Prummer, C. G. Hübner, B. Sick, B. Hecht, A. Renn, and U. P. Wild, "Single-Molecule Identification by Spectrally and Time-Resolved Fluorescence Detection," *Anal. Chem.* **72**, 443–447 (2000).
- [68] J. R. Lakowicz, *Principles of Fluorescence Spectroscopy* (Plenum Press, New York, 1983).
- [69] P. C. Schneider and R. M. Clegg, "Rapid Acquisition, Analysis, and Display of Fluorescence Lifetime-Resolved Images for Real-Time Applications," *Rev. Sci. Instr.* **68**, 4107–4119 (1997).
- [70] R. Ballew and J. N. Demas, "An Error Analysis of the Rapid Lifetime Determination Method for the Evaluation of Single Exponential Decays," *Anal. Chem.* **61**, 30–33 (1989).
- [71] W. Lukosz and R. Kunz, "Light Emission by Magnetic and Electric Dipoles Close to a Plane Interface. I. Total radiated Power," *J. Opt. Soc. Am.* **67**, 1607–1613 (1977).
- [72] J. D. Jackson, *Classical Electrodynamics* (Wiley & Sons, New York, 1962).
- [73] L. Novotny, "Allowed and Forbidden Light in Near-Field Optics. I. A Single Dipolar Light Source," *J. Opt. Soc. Am. A* **14**, 91–104 (1997).
- [74] A. Harootunian, E. Betzig, A. Muray, A. Lewis, and M. Isaacson, "Near-Field Investigation of Submicrometer Apertures at Optical Wavelengths," Abstract 1984 Annual Meeting of the Optical Society of America p. 1293 (1984).

- 
- [75] E. Betzig, J. Trautman, R. Wolfe, E. Gyorgy, P. Finn, M. Kryder, and C. Chang, "Near-Field Magneto-optics and High-Density Data-Storage," *Appl. Phys. Lett.* **61**, 142–144 (1992).
- [76] J. Trautman, J. Macklin, L. Brus, and E. Betzig, "Near-Field Spectroscopy of Single Molecules at Room-Temperature," *Nature* **369**, 40–42 (1994).
- [77] B. Knoll and F. Keilmann, "Near-Field Probing of Vibrational Absorption for Chemical Microscopy," *Nature* **399**, 134–137 (1999).
- [78] E. Sanchez, L. Novotny, and X. Xie, "Near-field microscopy based on two-photon excitation with metal tips," *Phys. Rev. Lett.* **82**, 4014–4017 (1999).
- [79] J. Azoulay, A. Debarre, A. Richard, and P. Tchenio, "Optical Contrast in Apertureless Microscopy," *Appl. Opt.* **39**, 129–134 (2000).
- [80] N. Hayazawa, Y. Inouye, and S. Kawata, "Evanescent field excitation and measurement of dye fluorescence in a metallic probe near-field scanning optical microscope," *J. Microsc.* **194**, 472–476 (1999).
- [81] H. Hamann, A. Gallagher, and D. Nesbitt, "Near-field fluorescence imaging by localized field enhancement near a sharp probe tip," *Appl. Phys. Lett.* **76**, 1953–1955 (2000).
- [82] Y. Martin, F. Zenhausern, and H. Wickramasinghe, "Scattering spectroscopy of molecules at nanometer resolution," *Appl. Phys. Lett.* **68**, 2475–2477 (1996).
- [83] T. Yang, G. Lessard, and S. Quake, "An Apertureless Near-Field Microscope for Fluorescence Imaging," *Appl. Phys. Lett.* **76**, 378–380 (2000).
- [84] J. Pedarnig, M. Specht, and T. Hänsch, "Fluorescence Lifetime Variations and Local Spectroscopy in Scanning Near-Field Optical Microscopy," *Photons and Local Probes*, eds. O. Marti, R. Möller pp. 151–163 (1995).
- [85] D. Pastré, P. Grossel, and M. Troyon, "Fluorescence Imaging in Near-Field Optical Microscopy: Influence of the Molecule Excitation Rate," *Optics Communications* **156**, 92–100 (1998).





## Werner Trabesinger

### *Date and Place of Birth*

3 October 1973, Klagenfurt, Austria.

### *Education*

1992 - 1995 Study of Physics at the Technical University of Vienna, Austria.

1995 - 1997 Study of Physics at the University of Linz, Austria.

1998 Diploma in Physics. Thesis: *Single Molecule Microscopy in Biosystems. Photobleaching and Colocalization Studies*. The work was supervised by Th. Schmidt and carried out at the Institute for Biophysics at the University of Linz.

1997 - present Ph.D. thesis in the group of Professor Urs P. Wild in the Physical Chemistry Laboratory at the Swiss Federal Institute of Technology (ETH) in Zürich, Switzerland.

### *Appointments*

Research Assistant in Physical Chemistry at the ETH, 1997 - 2001.

Teaching Assistant for a variety of Physical Chemistry lectures and laboratory courses at the ETH, 1997 - 2001.